Journal of Rock Mechanics and Geotechnical Engineering 16 (2024) 961–978

Contents lists available at ScienceDirect

Journal of Rock Mechanics and Geotechnical Engineering

journal homepage: www.jrmge.cn

Full Length Article

A process-oriented approach for identifying potential landslides considering time-dependent behaviors beyond geomorphological features

Xiang Sun [a], Guoqing Chen [a,*], Xing Yang [a], Zhengxuan Xu [b], Jingxi Yang [c], Zhiheng Lin [b], Yunpeng Liu [c]

[a] State Key Laboratory of Geohazard Prevention and Geoenvironment Protection, Chengdu University of Technology, Chengdu, 610059, China
[b] China Railway Eryuan Engineering Group Co. Ltd., Chengdu, 610031, China
[c] Power China Chengdu Engineering Co. Ltd., Chengdu, 610072, China

ARTICLE INFO

Article history:
Received 16 January 2023
Received in revised form
17 March 2023
Accepted 15 May 2023
Available online 6 August 2023

Keywords:
Geomorphological features
Evolution history
Time-dependent stability calculation
Landslides identification
Qinghai-Tibet Plateau

ABSTRACT

Geomorphological features are commonly used to identify potential landslides. Nevertheless, overemphasis on these features could lead to misjudgment. This research proposes a process-oriented approach for potential landslide identification that considers time-dependent behaviors. The method integrates comprehensive remote sensing and geological analysis to qualitatively assess slope stability, and employs numerical analysis to quantitatively calculate aging stability. Specifically, a time-dependent stability calculation method for anticlinal slopes is developed and implemented in discrete element software, incorporating time-dependent mechanical and strength reduction calculations. By considering the time-dependent evolution of slopes, this method highlights the importance of both geomorphological features and time-dependent behaviors in landslide identification. This method has been applied to the Jiarishan slope (JRS) on the Qinghai-Tibet Plateau as a case study. The results show that the JRS, despite having landslide geomorphology, is a stable slope, highlighting the risk of misjudgment when relying solely on geomorphological features. This work provides insights into the geomorphological characterization and evolution history of the JRS and offers valuable guidance for studying slopes with similar landslide geomorphology. Furthermore, the process-oriented method incorporating time-dependent evolution provides a means to evaluate potential landslides, reducing misjudgment due to excessive reliance on geomorphological features.

1. Introduction

The Qinghai-Tibet Plateau has experienced continuous uplift and compressional structural deformation since the Cenozoic Era due to the ongoing compression of the Indian and Eurasian plates. This region exhibits complex topography and geomorphology (Yang et al., 2016; Zhang et al., 2016), active plate tectonics (Tapponnier and Molnar, 1977; Zhang et al., 2004; Cai et al., 2016; Ding et al., 2017), high seismic intensity (Xu et al., 2016), and prevalent mountain disasters (Cui et al., 2015). The development of geological hazards on the Qinghai-Tibet Plateau is influenced by the dynamic coupling of plate compression, plateau uplift, climate change, and engineering forces. This interaction results in a high density of geological hazards with significant damage (Huang, 2012). Typical geological hazards include the Yigong landslide in Bomi County, Tibet, in 2000 (Shang et al., 2003), the Xinmo Village landslide in Maoxian County in 2017 (Fan et al., 2017; Intrieri et al., 2018), and the Baige landslide in Jiangda County, Tibet, in 2018 (Cai et al., 2020). These geological hazards often cause a series of disaster chains (Fan et al., 2021; Wang et al., 2021). Current research on major geological topics of the Qinghai-Tibet Plateau mainly focuses on large-scale landslides and debris flows (Lu and Cai, 2019), giant deposits of complex origin, ultra-large rock debris slopes, plateau ice and snow disasters (Kuang and Jiao, 2016; Niu et al., 2016; Zhang et al., 2020), high-temperature heat damage (Guo et al., 2017; Jiang et al., 2019; Mao et al., 2021), high in situ stress (Wang et al., 2020), and plateau karst (Sun et al., 2016). In particular,

* Corresponding author.
E-mail address: chgq1982@126.com (G. Chen).
Peer review under responsibility of Institute of Rock and Soil Mechanics, Chinese Academy of Sciences.

https://doi.org/10.1016/j.jrmge.2023.05.014

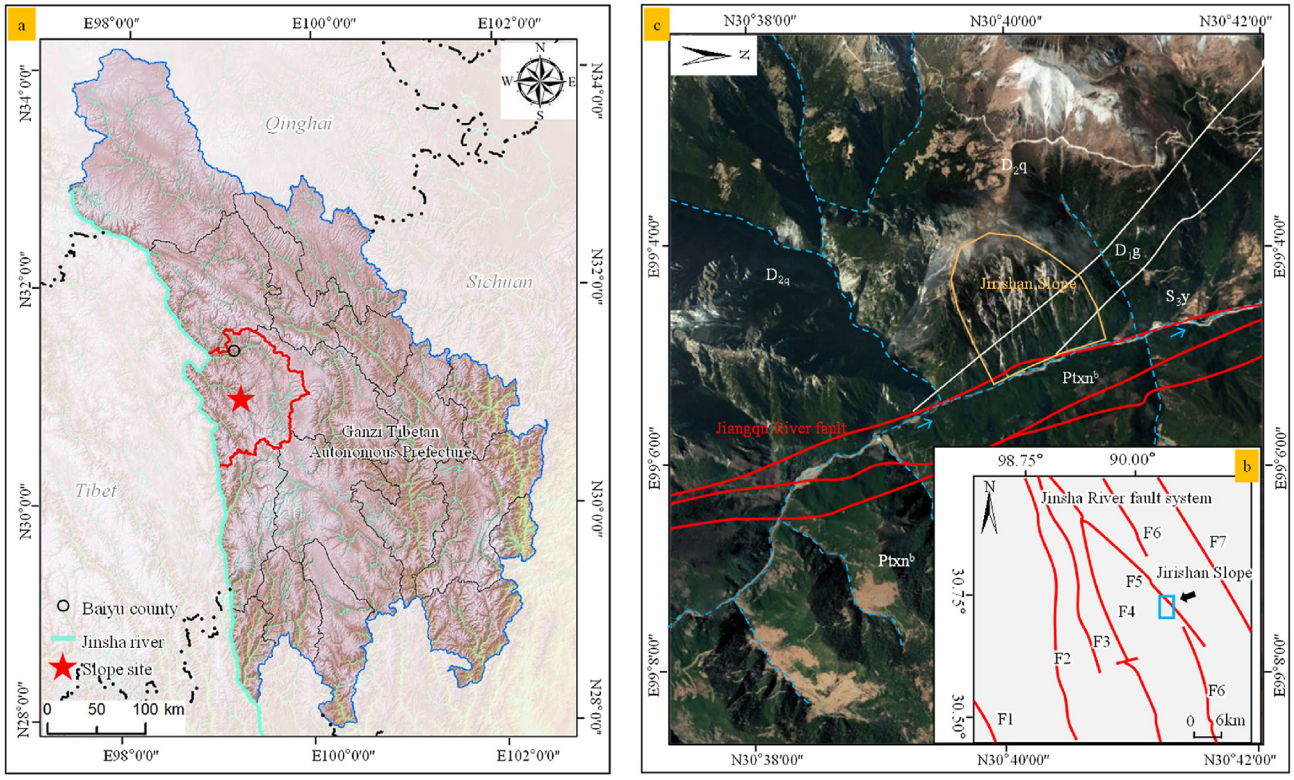

Fig. 1. (a) Geographical location of the Jiarishan slope (JRS). (b) Geological settings of the Jinsha River fault system. (c) Geological settings of the JRS.

extensive research has been conducted on the geological conditions, formation mechanisms, and prevention measures of various geological hazards that occur in the region (Shang et al., 2003; Fan et al., 2017; Cai et al., 2020; Wang et al., 2023). However, there is relatively less research focused on potential hazards that do not yet occur. Nevertheless, recognizing the early signs of potential hazards and implementing preventive measures to avoid major engineering projects intersecting with slopes prone to deformation can significantly mitigate the impact of geological hazards on such projects (Ji et al., 2020; Prakash et al., 2020).

In early recognition, optical remote sensing is the most commonly used technology (Metternicht et al., 2005; Nichol et al., 2006). In recent years, interferometric synthetic aperture radar (InSAR), light detection and ranging (LiDAR), laser doppler vibrometer terrestrial laser scanning (TLS), and unmanned aerial vehicle (UAV) have also been used for geohazard identification and have been rapidly developed (Ferretti et al., 2000; Berardino et al., 2002; Zhang et al., 2012; Hsieh et al., 2016; Mateos et al., 2017; Jia et al., 2019; Li et al., 2020; Xie et al., 2022). When employing these methods for landslide identification, geomorphological features are typically the primary criterion for assessing whether a slope has the potential for landslides. However, relying solely on geomorphological features to determine the potential for landslides can lead to a high possibility of misjudgment in the complex geological context of the Qinghai-Tibet Plateau. Therefore, additional engineering geological surveys and analysis of the slope's evolutionary history are necessary. It is important to acknowledge that even a stable slope may exhibit landforms resembling landslides, and this possibility cannot be ignored (Scaioni et al., 2014; Fan et al., 2017; Intrieri et al., 2018; Ouyang et al., 2018; Li et al., 2019).

In the Jinsha River basin on the Qinghai-Tibet Plateau, there is a recently constructed tunnel known as the Jiarishan tunnel, with an associated slope at the tunnel entrance referred to as the Jiarishan slope (JRS). Based on satellite remote sensing data, the trailing edge of the JRS exhibits a circular chair-shaped landform, resembling the scarp of a landslide. Considering that the slope is anti-dip in nature, there is a possibility of toppling deformation and instability (Guo et al., 2020). In order to overcome the limitations of relying solely on geomorphological features for landslide identification, a process-oriented method considering time-dependent evolution is applied to assessing the potential landslide status of the JRS in this study. The application of this method reveals that the JRS, despite exhibiting landslide geomorphology, is considered as a stable anti-dip slope. This highlights the importance of considering time-dependent evolution in the assessment of potential landslides, as it provides a more comprehensive understanding of slope stability. This work provides insights into the slope geomorphology and evolution history of the JRS as well as useful inspiration for the study of other slopes with similar landslide geomorphology in the Qinghai-Tibetan Plateau. Furthermore, the proposed process-oriented method, which takes into account time-dependent evolution, provides a valuable approach for evaluating the potential of a slope to experience landslides.

2. Study area and geological settings

The JRS is situated in Baiyu County, located in the Qinghai-Tibet Plateau of China. It is part of the Jinsha River fault system, as depicted in Fig. 1a and b. The Jinsha River fault system, situated on the eastern margin of the Qinghai-Tibetan Plateau, is characterized by complex geological structures. The formation of the Qinghai-Tibetan Plateau occurred around 70 million years ago as a result of the collision between the Indian and Eurasian plates. This collision led to crustal shortening and the development of thrusts and deformations in the collision zone during the Eocene period. The tectonic activity in the eastern region of the Jinsha River fault

system resulted in the formation of the Songpan-Ganzi trough fold and fault system, while the western region gave rise to the Sanjiang trough fold system.

The near-field region is characterized by relatively developed fault structures. From west to east, the main faults in this area include the Shengen-Zhongmei fault (F1), Polo-Muxie fault (F2), Romer-Ani fault (F3), Zhuying-Shanyan fault (F4), Polo-Sama fault (i.e. Jiangqu River fault) (F5), Azuo-Rannei fault (F6), and Mount Ella fault (F7). Details on the occurrence, activity, and category of these faults can be found in Table 1.

Fig. 1c depicts the geological context of the JRS. An NNW-oriented fault (F5) with a length exceeding 120 km is presented along the Jiangqu River at the base of the slope. The fault strikes N20-30°W/SW and dips 55–70°SW. The fault zone has an approximate width of 100 m and follows the Daxinong-Jiangqu valley. It dips in southwest direction and is characterized by distinctive geomorphological features and inclinations ranging from 50° to 70°. The fault was active during the Early to Middle Pleistocene epoch, but showed a reduced activity since the Late Pleistocene. Quartz within the fault zone displays a simple morphology and does not exhibit well-developed crustal quartz formations. Eroded quartz (orange peel, scaly, and mossy quartz) constitutes 70%–90% of the quartz presented. ESR dating of fractured quartz yields an age of (37.1 ± 3) million years.

The exposed slope strata primarily consist of black carbonaceous crystalline limestone, argillaceous dolomite, quartz shallow granulite with iron dolomite, and schist from the Silurian Yongren Formation (S_3y). The limestone and dolomite are dense, hard, and relatively intact with individual layer thickness of 20–100 cm. Surface weathering imparts a grayish-white coloration and the rock mass is partially fragmented. Fractures predominantly occur along bedding planes and joints. Fault F5 locally disrupts the rock mass and dissolution cavities occasionally form at the intersection of syntectonic cracks and joint planes with widths of 50–120 cm, heights of 40–70 cm, and depths of 50–100 cm. The Devonian Gerong Formation (D_1g) comprises massive light-yellow dolomite and dolomitic limestone that are dense, hard, and blocky with an intact appearance. The Devonian Qiongcuo Formation (D_2q) contains thick-massive crystalline limestone, biological limestone, fine-grained dolomite, and dolomitic limestone with minor argillaceous limestone and shale. The limestone and dolomite are dense, hard, and relatively intact with individual layer thicknesses exceeding 50 cm. Slope residual overburden (Q_4^{dl+el}) occurs above an elevation of 4418 m, while slope collapse overburden (Q_4^{col+dl}) occurs below an elevation of 3600 m and primarily consists of gravelly soil with a thickness of 5–20 m.

Table 1
The main faults and their properties in the JRS region.

Fault	Structure and attitude	Extension length (km)	Main active era	Category
F1	N30°-60°W/SW(NE) ∠60°–75°	–	Q_3	Reverse fault
F2	SN	150	Q_2	Reverse fault
F3	NW/SW∠60°–80°	>120	Q_3	Strike-slip fault
F4	NNW/NE(SW) ∠50°–75°	80	Before Q_1	Thrust fault
F5	NW/SW∠50°–70°	60	–	Reverse fault
F6	NW	–	Q_2	Reverse fault
F7	NW	65	Q_2	Right-handed thrust fault

3. Methods and materials

3.1. Methods

Considering that the use of remote sensing methods to identify potential landslides generally focuses on the geomorphological features of the slope, emphasis on the geomorphological features will sometimes lead to misjudgment. The purpose of rapid identification can be achieved using advanced technical means. Nevertheless, conventional geological tools such as field-based geological surveys, rock mass structure surveys and geological history analysis can also be used. Then, a process-oriented method considering time-dependent evolution for potential landslide identification is established. The process includes comprehensive remote sensing identification, comprehensive geological identification and numerical analysis, as shown in Fig. 2.

The proposed process-oriented method for potential landslide identification encompasses the following steps:

(1) Comprehensive remote sensing is used to initially determine whether the slope is potentially stable;
(2) The possible potential failure modes combined with the geomorphological features and stratigraphic lithology are listed;
(3) Comprehensive geology is used to further determine whether the slope is a potential landslide;
(4) Numerical analysis is used to calculate the time-dependent evolution process and the aging stability of slopes;
(5) A comprehensive determination is made concerning the potential for a slope that may experience landslides by integrating the results obtained from the remote sensing analysis, comprehensive geological investigations, and numerical analysis.

By considering both qualitative and quantitative factors, a more accurate assessment of the slope's potential as a landslide can be obtained. The method can avoid the shortcomings of remote sensing methods that focus on geomorphic features and ignore geological history, geological conditions, and rock mass structure. The method aims to reduce the rate of misjudgment caused by an excessive reliance on geomorphological features.

3.1.1. Comprehensive remote sensing for preliminary judgment of stability

Comprehensive remote sensing includes analyzing the current landform characteristics and landform zoning using UAV, comparing the evolution of historical landforms using remote sensing images of historical sequences, analyzing the trend of surface deformation, and judging the surface deformation quantitatively using InSAR. By integrating UAV, remote sensing and InSAR data, a comprehensive preliminary judgment can be made.

Satellite-based synthetic aperture radars (SARs) commonly employ C-, X-, and L-band sensors. This study utilizes data from the European Space Agency (ESA)'s Sentinel-1 satellite, which carries a C-band sensor with a wavelength of 5.6 cm. The SAR data set comprises over 50 phases of Sentinel-1 data, with ascending phase data fully covering the study area. Data were acquired between November 2017 and November 2020 and processed using the Satellite-Based Augmentation System Small Baseline Subset (SBAS-InSAR) technique. Remote sensing image data were obtained from Google Earth and GF-2 satellites for the period of 1985–2020. UAV data were collected in August 2020.

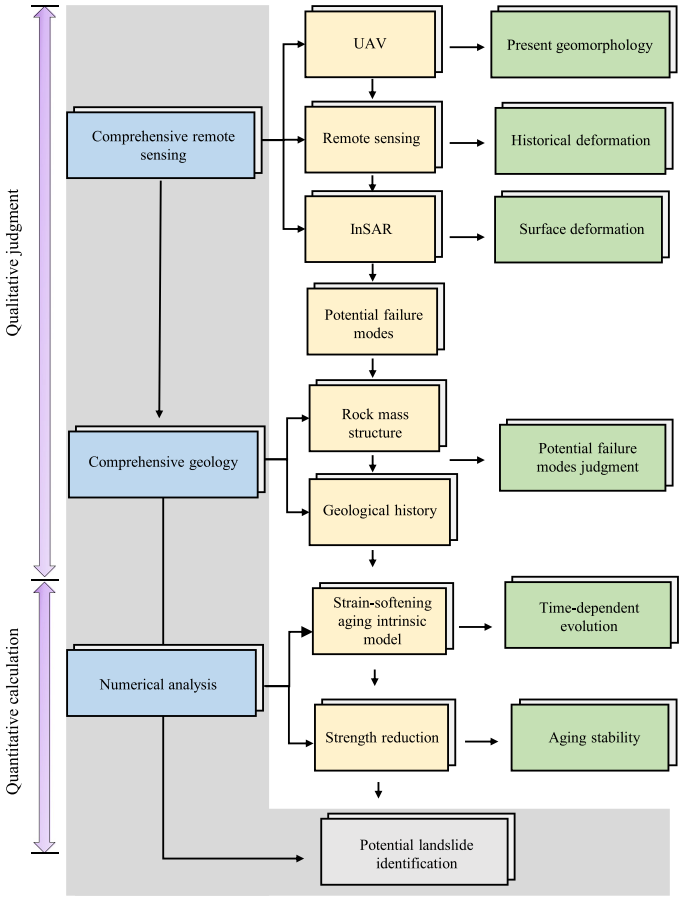

Fig. 2. The process-oriented method considers time-dependent evolution to evaluate whether a slope is a potential landslide.

3.1.2. Comprehensive geology for further judgment of stability

Comprehensive geology involves utilizing the characteristics of rock mass structure obtained through field investigations to assess whether the potential failure mode has been established. Furthermore, it entails analyzing the process of geomorphic evolution and examining the geological evolution history to uncover the underlying factors responsible for the formation of the current geomorphology. By integrating information on rock mass structure and geological evolution history, a comprehensive geological judgment is made, providing a holistic understanding of the slope's geological dynamics and landscape evolution.

On-site investigations were conducted to study the geomorphology of the ground and the rock mass structure inside the slope. Field mapping was performed using 1:1000-scale geological maps, a handheld global positioning system (GPS), a laser rangefinder, and a compass. Geophysical methods, including resistivity measurements, were employed to enhance the investigation. To gain insights into the material composition of specific geomorphic areas, four trial trenches and one adit were excavated. Field surveys were conducted using GPS, laser rangefinders, and compasses to accurately determine the spatial distribution, orientation, and size of prominent landforms, as well as to identify signs of toppling failure along the slope. Resistivity measurements played a crucial role in identifying distinctive landforms such as scarps and karst formations. The trial trenches provided valuable information concerning the material composition of specific geomorphic areas, while the adit allowed for a detailed examination of signs of toppling failure from the surface to the interior of the slope.

3.1.3. Strain-softening aging intrinsic model for time-dependent mechanical calculation

The strain-softening model is concatenated with the Burgers model to form the strain-softening aging intrinsic model capable of simulating the viscoelastic-plastic behavior of the material. It considers the rock mass rheological properties and degradation properties during the downcutting process of valleys (Itasca, 2005; Sun et al., 2023). The rheological equation corresponding to the strain-softening aging intrinsic model can be expressed as

$$\varepsilon = \frac{\sigma}{E_{\mathrm{M}}} + \left(\frac{\sigma}{\eta_{\mathrm{M}}}\right)t + \frac{\sigma}{E_{\mathrm{K}}}\left(1 - e^{\frac{E_{\mathrm{K}}}{\eta_{\mathrm{K}}}t}\right) + \varepsilon^{\mathrm{p}} \tag{1}$$

where ε is the total strain, t is the time, σ is the stress, E_{M} is the elastic modulus of Maxwell body, η_{M} is the viscosity coefficient of Maxwell body, E_{K} is the elastic modulus of Kelvin body, η_{K} is the viscosity coefficient of Kelvin body, and ε^{p} is the strain of plastic body.

Kelvin, Maxwell, and plastic body contributions to stresses and strains are labeled using the superscripts K, M and P, respectively. Thus, the deviatoric behavior can be characterized by (Sun et al., 2023):

(1) Strain rate partitioning

$$\dot{e}_{ij} = \dot{e}_{ij}^{K} + \dot{e}_{ij}^{M} + \dot{e}_{ij}^{P} \tag{2}$$

(2) Kelvin body

$$S_{ij} = 2\eta_K \dot{e}_{ij}^{K} + 2G_K e_{ij}^{K} \tag{3}$$

(3) Maxwell body

$$\dot{e}_{ij}^{M} = \frac{\dot{S}_{ij}}{2G_M} + \frac{S_{ij}}{2\eta_M} \tag{4}$$

(4) S–S model

$$\dot{e}_{ij}^{P} = \lambda \frac{\partial g}{\partial \sigma_{ij}} - \frac{1}{3}\lambda\left(\frac{\partial g}{\partial \sigma_{11}} + \frac{\partial g}{\partial \sigma_{22}} + \frac{\partial g}{\partial \sigma_{33}}\right)\delta_{ij} \tag{5}$$

where e_{ij} is the deviator strain; $\dot{e}_{ij}$ is the deviator strain rate; S_{ij} is the deviator stress; $\dot{S}_{ij}$ is the deviator stress rate; G_M is the shear moduli of Maxwell body; G_K is the shear moduli of Kelvin body; g is the plastic potential function; λ is the plastic multiplier; σ_{11}, σ_{22} and σ_{33} are the maximum, intermediate and minimum principal stresses, respectively; $\dot{e}_{ij}^{K}$, $\dot{e}_{ij}^{M}$, and $\dot{e}_{ij}^{P}$ are the deviator strain rates of Kelvin, Maxwell, and plastic body, respectively.

In the strain-softening aging intrinsic model, the degradation process of strength parameters is expressed as a function related to plastic strain. The degradation of strength parameters including the cohesive force (c), the tensile strength (σ_t) and the angle of internal friction (φ) of material degrade in relation to corresponding increments in plastic strain:

$$\left.\begin{aligned} c &= c(\varepsilon^{ps}) \\ \varphi &= \varphi(\varepsilon^{ps}) \\ \sigma_t &= \sigma_t(\varepsilon^{pt}) \end{aligned}\right\} \tag{6}$$

where ε^{pt} and ε^{ps} are the cumulative values of the tensile and shear plastic strain, respectively.

To simplify calculations, multi-section linear functions are frequently used to approximate the degradation of rock mass strength parameters. The degradation curve is shown in Fig. 3. The numerical simulation incorporates the mechanical parameters of the rock mass obtained from a series of mechanical tests (see Table 2). For the stratification analysis, a conventional Coulomb slip model with area contact is adopted, which involves five key parameters: cohesion, angle of internal friction, tensile strength, normal stiffness (k_n), and shear stiffness (k_s). The normal stiffness is determined by (Cho et al., 2007) (see Table 3):

$$k_n = n\left(\frac{K + 4/3G}{\Delta Z_{min}}\right) \tag{7}$$

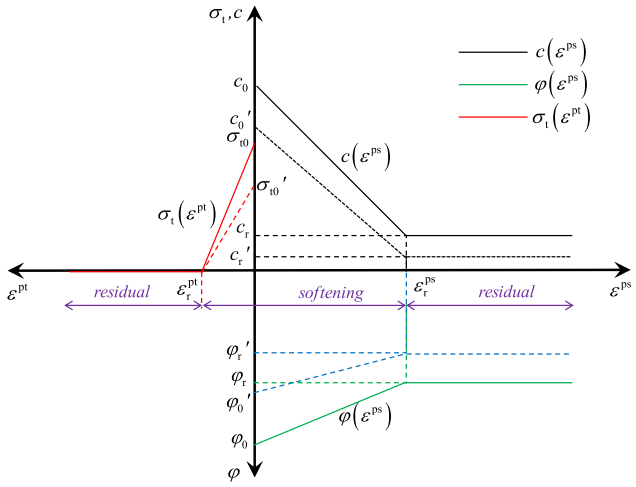

Fig. 3. Deterioration curve of rock mass strength parameters in the strain-softening aging intrinsic model. , where ε_r^{ps} is the shear plastic strain threshold, $c(\varepsilon^{ps})$ is the cohesion degradation function, $\varphi(\varepsilon^{ps})$ is the internal friction angle degradation function, ε_r^{pt} is the tensile plastic strain threshold, $\sigma t(\varepsilon^{pt})$ is the tensile strength degradation function, c_0 is the initial cohesion, c_r is the residual cohesion, φ_0 is the initial internal friction angle, φ_r is the residual friction angle corresponding to the shear plastic strain threshold, σ_{t0} is the initial tensile strength corresponding to the tensile plastic strain threshold, c_0', c_r', φ_0', φ_r', σ_{t0}' are the corresponding mechanical parameters after strength reduction of c_0, c_r, φ_0, φ_r, σ_{t0}, respectively.

Table 2
The mechanical parameters of rock masses.

Parameter	Value	
	Rock mass	Faults
ρ (kg m^{-3})	2650	2200
E (GPa)	16	4
μ	0.25	0.35
G_M (GPa)	6.4	1.48
η_M (GPa d)	12.8	2.96
G_K (GPa)	5.12	1.18
η_K (GPa d)	50	14.8
c_0 (MPa)	1.8	0.1
c_r (MPa)	0.5	0.1
φ_0 (°)	55	30
φ_r (°)	35	30
σ_{t0} (MPa)	1.5	0
ε	0.02	0.02
ε	0.001	0.001

Table 3
The mechanical parameters of stratification.

Parameter	Value
k_n (GPa m)	2
k_s (GPa m)	1.5
c (MPa)	0.1
φ (°)	30
σ_t (MPa)	0

where ΔZ_{min} is the minimum width of the area adjacent to the contact surface in vertical direction, n is the minimum size of the adjacent unit, K is the bulk modulus, and G is the shear modulus.

The strain-softening aging intrinsic model employs the Mohr–Coulomb yield criterion to account for tensile-shear failure. The stress threshold (i.e. σ_r) is related to the plastic strain (i.e. ε^{ps} and ε^{pt}), allowing the yield criterion to be expressed as:

$$\left.\begin{aligned} f^{s} &= \sigma_1 - \sigma_3 N_{\varphi(\varepsilon^{ps})} + 2c(\varepsilon^{ps})\sqrt{N_{\varphi(\varepsilon^{ps})}} = 0 \\ f^{t} &= \sigma_3 - \sigma_t(\varepsilon^{pt}) = 0 \end{aligned}\right\} \tag{8a}$$

$$N_{\varphi(\varepsilon^{ps})} = \frac{1+\sin[\varphi(\varepsilon^{ps})]}{1-\sin[\varphi(\varepsilon^{ps})]} \tag{8b}$$

where f^{s} is the shear yield function; f^{t} is the tensile yield function; and σ_3 and σ_1 are the maximum and minimum principal stress, respectively. The compressive stress is negative, and it is assumed that $\sigma_1 \leq \sigma_3$ in the model.

3.1.4. Strength reduction method for aging stability calculation

Based on the time-dependent calculation, the stability of a slope with different creep times is calculated using the strength reduction method. This process is implemented in three-dimensional distinct element code (3DEC). As illustrated in Fig. 3, strength reduction is done on an equal percentage basis. When the ratio of the maximum unbalance force at the differential nodes to the characteristic force of the system is greater than 10^{-5}, the block system is considered unbalanced and the discount factor at this time represents the stability factor of the slope. The stability factor is defined in Eq. (9) when considering the influence of the joints (Chen et al., 2021):

$$F_s = K_s = \frac{c}{c'} = \frac{\tan\varphi}{\tan\varphi'} = \frac{\sigma_t}{\sigma_t'} = \frac{c_j}{c_j'} = \frac{\tan\varphi_j}{\tan\varphi_j'} \tag{9}$$

where, F_s is the stability factor; K_s is the discount factor; c_j is the cohesion of the joint; φ_j is the angle of internal friction of the joints; c', φ', σ_t', c_j' and φ_j' are the cohesion of the rock mass, the angle of internal friction of the rock mass, the tensile strength of the rock mass, the cohesion of the joint, and the angle of internal friction of the joint after the plastic zone is exactly penetrated, respectively.

The process of evaluating the aging stability is as follows (see Fig. 4):

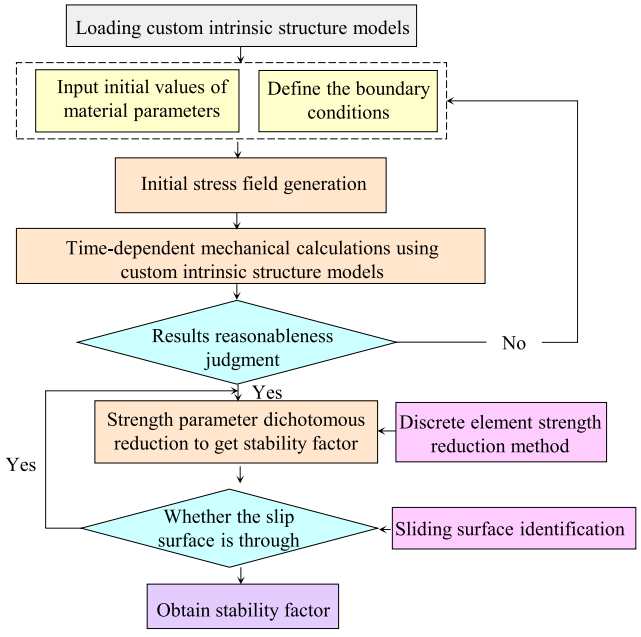

Fig. 4. Process of calculating the aging stability of slopes using the strength reduction method.

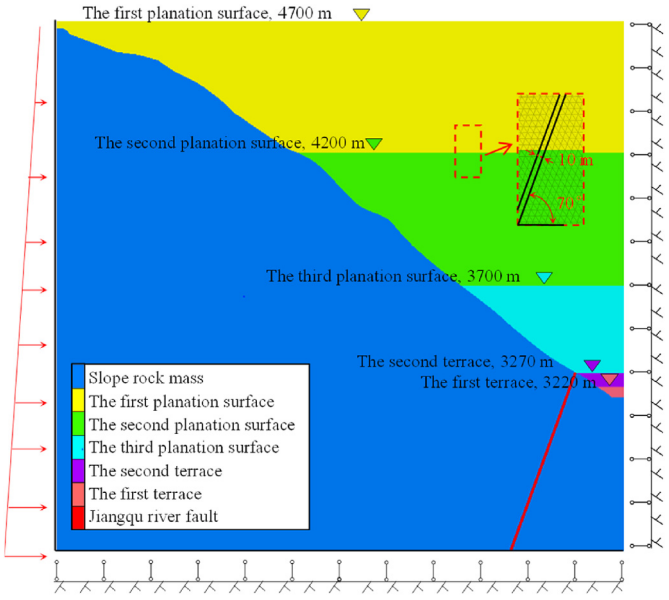

Fig. 5. Geometrical model, computational mesh and boundary condition.

(1) Load the strain-softening aging intrinsic model, and define the boundary and initial conditions, and material parameters.
(2) Using the strain-softening aging intrinsic model, calculate the time-dependent mechanical behavior to obtain the stress, strain, plastic zone, and displacement characteristics of the slope at different creep times.
(3) In Step (2), the measured in situ stress data are used to compare with the stress data obtained from the simulation in order to discern the reasonableness of the calculated results in Step (2). Check whether the calculated results in step (2) are reasonable, and if not, repeat Steps (1), (2), and (3) until the results are reasonable and obtain the calculation results.
(4) Using the strength reduction method, the tensile strength, cohesion, and angle of internal friction of the rock mass, as well as the cohesion and angle of internal friction of the joints, are simultaneously reduced based on the calculation from Step (3). This reduction is performed on different strain states, as illustrated in Fig. 3.
(5) Use a dichotomous method for strength reduction and stop calculations when a sliding surface forms from a penetrating damage zone to obtain the stability factor of slope.
(6) Obtain the location of the potential sliding surface of the slope and end the evaluation of aging stability.

3.2. Numerical model

In the numerical calculation, a model is established based on the engineering geological profile. The computational mesh is divided into three parts, i.e. slope rock mass, undercut part of the river valley, and fault. The model has dimensions of 2140 m in length and 2000 m in height. The rock strata are spaced 10 m apart and dip at an angle of 70°. The fault has a thickness of 15 m within the model. The initial shape of the model represents the river valley at the time of its first planation surface (see Fig. 5), and the whole process from the first planation surface to the current valley is simulated through five sequential denudations and undercuts (Ning et al., 2021). The depth of each stage of excavation is determined according to the regional river terrace elevations, which are 4700 m, 4200 m, 3700 m, 3270 m and 3220 m from the first planation surface to the

current valley, respectively. After each stripping undercutting calculation confirms stability, further stripping undercutting is carried out. Once valley undercutting calculations are completed, aging stability calculations are performed.

The boundary conditions consider the effects of both gravity and tectonic stress. Multiple simulations using different boundary condition models were conducted (Wang and Ma, 1986; Zhao et al., 2012) (see Fig. 6). The results revealed that the simulation data exhibited the closest match to the measured in situ stress data when vertical displacement and velocity constraints were enforced at the bottom of the model. The horizontal displacement and velocity constraints were imposed on the valley side of the model, and tectonic stress increased linearly with depth on the opposite side of the model (reaching 27 MPa at the bottom).

4. Results

4.1. Preliminary judgment based on comprehensive remote sensing

4.1.1. Geomorphology zonation based on UAV

The chair-shaped JRS is clearly visible in the image shown in Fig. 7. The elevation of the slope's summit is approximately 4545 m, while the elevation at the base of the slope ranges from 3170 m to 3200 m. The total area of the slope covers approximately 9 km^2. According to the deformation of the slope and the spatial distribution of karst, the JRS can be divided into three regions in plan view (see Fig. 8a and b): the main deformation zone, karst zone, and superficial deformation zone. In the main deformation zone, there are multilevel scarps. The karst zone has a distribution of karst caves. The superficial deformation zone has some developed superficial slippery surfaces. The characteristics of these various parts will be discussed below.

(1) Main deformation zone

Above elevation 4400 m, the vegetation consists mainly of plateau grassland and shrubs. The terrain slope is generally between 15° and 20° and appears as a circular chair-shaped slumped landform with six levels of scarps. The height difference between the fourth and fifth scarps is relatively small, only 1–2 m. The grooves, 0.3–5 m in depth and 5–20 m in width, appear on all scarps except for the first level. The groove on the fifth level scarp is the deepest at 5 m and partially shows the scenario of reverse slope scarps. The resistivity measurement results indicate the presence of four fractures widening along the structural plane at the trailing edge of the larger four-level scarps. These fractures exhibit an average depth of 150 m (see Fig. 8). The circular chair-shaped back wall at the top exhibits heights ranging from approximately 35 m–45 m. On the southwest side, the back wall reaches heights of approximately 80 m–100 m, while on the northeast side, the back wall heights range from approximately 30 m–50 m. These observations suggest a migration trend from the southwest to the northeast. The back wall is subjected to freeze and thaw weathering, the exposed bedrock is broken, and the thickest part of the residual slope layer covering the surface is 15–20 m. The exploration trench reveals that the thickness of the residual slope deposits in the groove is generally 5–10 m (see Fig. 9).

(2) Karst zone

The process of karstification primarily occurs at elevations between 3900 m and 4400 m. Early karsts developed along structural planes and layers. During the development process of karstification, the soluble rock is chemically corroded by groundwater, and the weaker rocks have dissolved away, forming stone forests and stone walls (see Fig. 10). The stone forests and stone walls exhibit heights of more than tens of meters. Over time, these formations have been subjected to weathering, unloading, freezing and thawing, leading to erosion and destruction. As a result, some of these features have transformed into mound-like shapes, particularly the shorter, scattered, and isolated stone forests. At present, the remnants of early karst peaks and forests can still be clearly observed from the surface survey. The surface underwater seepage still has the effect of dissolving and widening the cracks. Nevertheless, this dissolution is more concentrated on the rock mass structure below the erosion base level.

The excavation of the trench at the rear edge of the slope exposed karst cracks and gray-green mud in the bedrock, which are associated with bauxite minerals and indicate a closed environment. At adit PDG01, located at an elevation of 3650 m, early karst

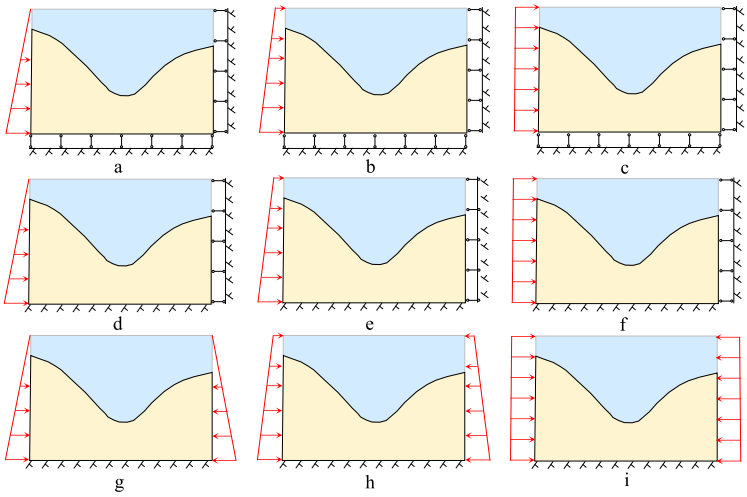

Fig. 6. Models with different boundary conditions: (a) Roller bottom and unilateral triangular distributed stress boundary conditions; (b) Roller bottom and unilateral trapezoidal distributed stress boundary conditions; (c) Roller bottom and unilateral rectangular distributed stress boundary conditions; (d) Fixed bottom and unilateral triangular distributed stress boundary conditions; (e) Fixed bottom and unilateral trapezoidal distributed stress boundary conditions; (f) Fixed bottom and unilateral rectangular distributed stress boundary conditions; (g) Fixed bottom and lateral triangular distributed stress boundary conditions; (h) Fixed bottom and lateral trapezoidal distributed stress boundary conditions; and (i) Fixed bottom and lateral rectangular distributed stress boundary conditions.

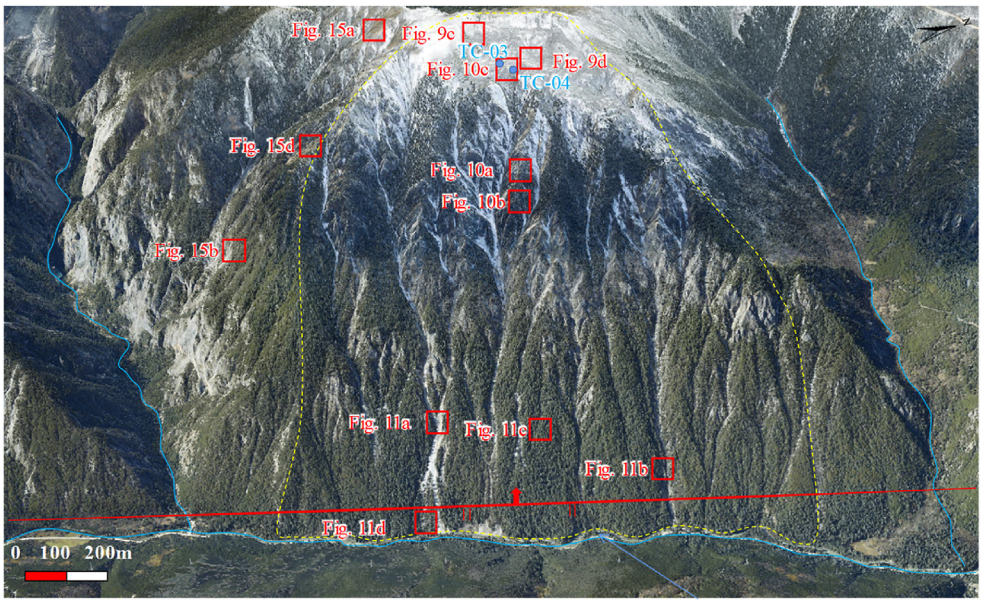

Fig. 7. Image of the JRS depicting its plan zonation.

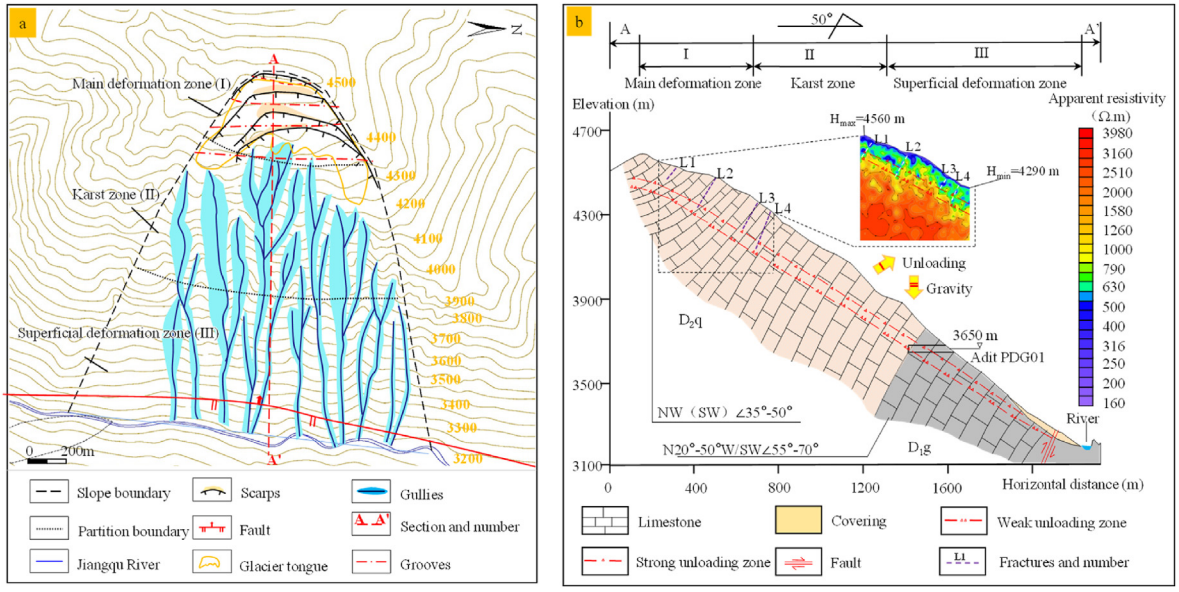

Fig. 8. (a) Sketch of the JRS reflecting the distribution of the major surface landforms and (b) longitudinal profile of the JRS.

cracks are observed in some sections. Analysis of twenty-four dissolution cracks within a 200 m range reveals that these cracks typically open between 0.5 cm and 2 cm, with a maximum width of 5 cm. The cracks exhibit grayish-yellow rock blocks, cuttings, and a calcium film, among other characteristics. The dissolution cracks are characterized by three-wall penetration and undulating roughness inside the adit. At present, groundwater in the adit is not developed, and there is a lack of new conditions for the development of karst cracks because the erosion base level of the Jiangqu River has dropped significantly.

(3) Superficial deformation zone

For the slope area below the 3600 m elevation range, the average slope angle is approximately 35°. The terrain is slightly undulating in this zone, and the surface vegetation is dense and dominated by perennial trees. There are many gullies on the slope surface, with different depths up to tens of meters deep, and the rock mass exposed on the sidewalls of the gullies has good integrity (see Fig. 11). According to the investigations, the scenario of saber trees appeared sporadically in this zone, which was caused by the partial slippage of the shallow overburden of the slope surface. The foot of the slope is affected by the scouring of the Jiangqu River, and there are many slippery and slumping scenarios on the slope surface. The slumping surface has a width of 10–60 m and a height of 30–50 m. In addition, it is affected by the erosion of the surface water flow, forming a river-across scouring gully. For instance, a groove developed on the downstream side of a slope, with a width of 10–20 m, is a seasonal gully.

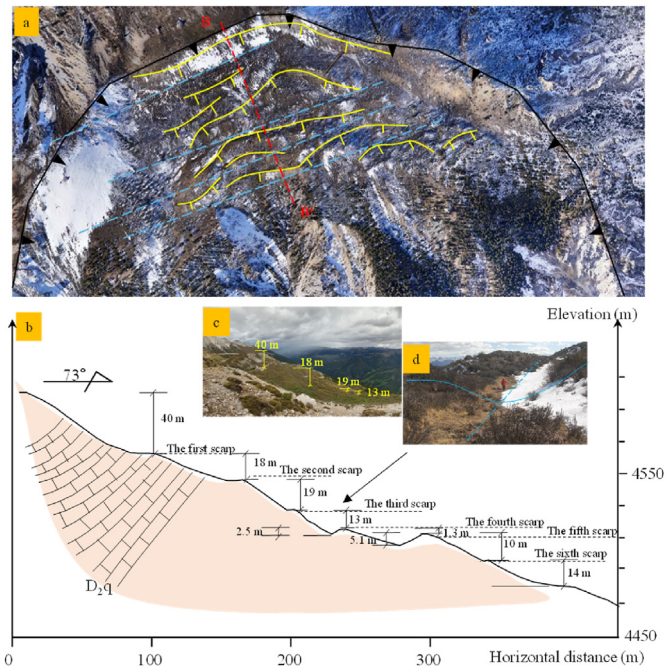

Fig. 9. Images and photos show the features of the landform in main deformation zone: (a) Image and floor plan of main deformation zone, (b) photos of scarps and grooves in main deformation zone, (c) the third scarp, and (d) longitudinal profile of main deformation zone.

4.1.2. Historical deformation analysis based on remote sensing

Remote sensing images from four different time periods were used for comparison, and the data sources and timings were described in the previous section. The chair-shaped terrain and the scarps of the trailing edge are presented in Fig. 12a. During these four periods, there was no obvious continuous deformation of the slope as a whole and the river channel at the foot of the slope showed almost no signs of being squeezed or diverted. The image shows that the superficial damage in the karst area has continued to develop on the surface of the slope, and that the exposed area of gray-white rock increased in size. To assess the presence of continuous overall deformation on the slope, specific regions along the back wall were selected, and the changes in their respective areas were analyzed. These areas include the one indicated by A-A′ on the right side of the back wall, the ones B—B′, D-D′, and E-E′ on the rear side of the back wall, and one C—C′ on the left side of the rear edge. Statistical analysis indicates that although there is a gradual increase in size for these areas along the back wall of the slope, the observed changes are relatively small (see Fig. 13).

4.1.3. Surface deformation analysis based on InSAR

The SBAS-InSAR time series analysis based on Sentinel-1 data is used to analyze the slope surface deformation. The acquisition time is from November 2017 to November 2020. The result shows that there is no obvious deformation of the slope (see Fig. 14).

In conclusion, the JRS displays typical features of a landslide landform. Persistent deformation was not detected through SBAS-InSAR analysis. Remote sensing images indicate the development of surface deformation in the karst areas of the slope, and the area of the back wall has shown continued growth. However, it should be noted that comprehensive remote sensing primarily considers surface and geomorphic characteristics, limiting its ability to assess internal conditions. Therefore, based on comprehensive remote sensing alone, it cannot definitively determine that the slope is not a potential landslide.

4.2. Potential failure modes

The joint cracks that developed on the JRS can be divided into primary joints and unloading cracks according to the genetic types. The primary joints are dominated by planes, and the planes are anti-dip and steep (N20°-50°W/SW∠55°—70°). Unloading cracks are mainly manifested as tensile cracks that are parallel to the bank slopes and inclined outside the slope. The trend of cracks is mainly NW. Based on survey results of joint cracks by adit and slope surface, the following five groups of joint cracks are observed (see Fig. 15). Joint crack group J1 was with the occurrence of N35°—60°W/NE∠71°—88°, and the extension greater than 2 m. The surface of J1 was rough, and the degree of weathering was mild to moderate rust staining. The opening of most cracks ranges from 0.1 cm to 0.5 cm, with some openings measuring between 1 cm and 5 cm. The occurrence of J2 is N70°—80°E/NW∠50°—60°, and these joint cracks extend more than 2 m. The surface is rough, and part of the structure surface forms step ridges. The degree of weathering was slight to moderate rust staining, with openings of 0—0.3 cm. The occurrence of J3 is E—W/N∠80°—90°, and these joint cracks extend 2—3 m. The surface is straight-undulating and rough, and the degree of weathering shows a mild-medium degree of rust staining, with openings of 0—0.3 cm. The occurrence of J4 is N5°—20°E(W)/NW(SW)∠35°—50°, and the extension of these joint cracks is more than 2 m. The surface is rough, and the degree of weathering is light-moderate rust staining, with openings of 0.1—0.5 cm. The occurrence of J5 was N5°—20°E(W)/NW(SW)∠60°—85°, and these joint cracks extended more than 2 m. The surface was rough, and the degree of weathering was mild-moderate rust staining, with openings of 0.1—0.5 cm.

It can be observed that all dominant structural planes of the JRS intersect with the slope direction at a significant angle, except for group J1 as shown in Fig. 15e. The inclination angles of all joint cracks, including group J1, are primarily medium to steep. This indicates that the two-by-two combination of superior structural surfaces does not provide a suitable sliding surface for plane sliding. Therefore, the failure mode can be considered as toppling failure. Based on L1-L4 in Fig. 8b, four shallow sliding surfaces (H1—H4) are identified based on the unstable sliding of the upper levels. Additionally, the H5 slip surface is defined by considering the creep deformation of the deeper layer, as shown in the schematic diagram in Fig. 16.

4.3. Further judgment based on comprehensive geology

4.3.1. Potential failure mode determination considering rock mass structure

Toppling failure is a common and serious instability scenario in both natural and artificial rock slopes (Tu and Deng, 2020). The toppling fracture mechanism has been studied at numerous sites, including road-cut slopes, hydropower high rock slopes, open pits, and natural steep slopes (e.g. De Freitas and Watters, 1973; Wyllie, 1980; Caine, 1982; Woodward, 1988; Cruden et al., 1993; Tamrakar et al., 2002).

Toppling failure models can be divided into two main categories (see Fig. 17). Bending-overturning-toppling failure typically occurs in soft rock slopes with high plasticity. The deformation process is slow and tends to stabilize gradually. Several examples of such failures include the Laxiwaguobu bank slope, the Miaowei Hydropower Station dam abutment slope, the slope of the diversion ditch of the Xiaowan Hydropower Station, the bank slope of the Santan section of Jinping I, the Huangdeng Hydropower Station #1 and #2 dumping bodies, and the Yalong River Hydrological Station. In contrast, massive toppling failure usually occurs in brittle hard rock

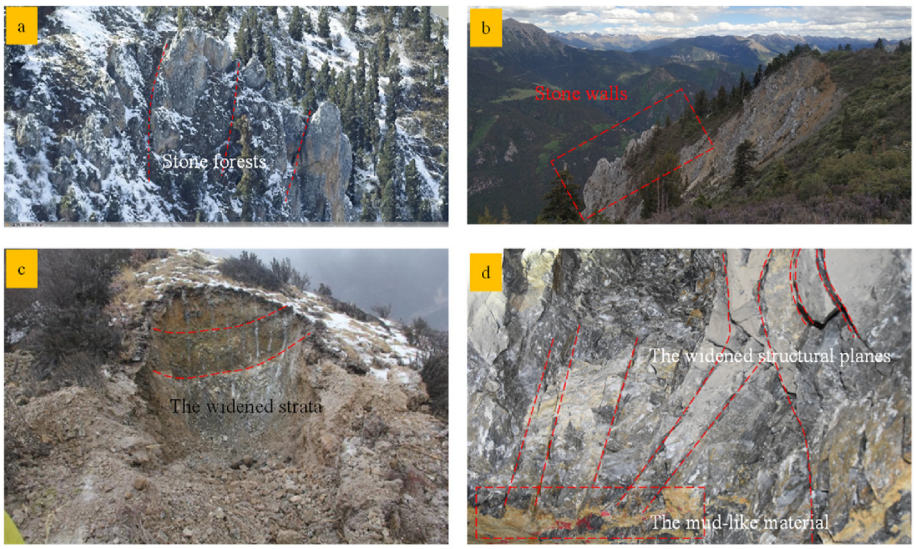

Fig. 10. Images and photos show the features of the landform in karst zone: (a) Stone caused by karstification; (b) Stone walls caused by karstification; (c) The widened strata formed by karstification; and (d) The widened structural planes and the mud-like material formed by karstification.

slopes, and the deformation is relatively large. This type of failure can quickly develop into a catastrophic landslide.

Previous studies have shown that most toppling fractures occur in the near-surface and shallow rock mass of slopes with a thickness of tens of meters (Zhang et al., 2015; Gu and Huang, 2016). However, in recent years, numerous cases of deep-seated toppling fractures with distances to the slope surface of 200–300 m have been recorded in Southwest China (Qi et al., 2004; Huang, 2012; Tu and Deng, 2020). Large-scale toppling failures in deep valleys typically undergo a prolonged incubation period and exhibit two distinct characteristics: significant variations in the dip angle of the strata and division of the deep-seated toppling rock mass into four zones, i.e. rock creep deformation zone, intense toppling zone, weak toppling zone, and parent rock zone, from the outer to the inner parts of the slope. However, the JRS slope does not display these typical characteristics. On the JRS, the deformation and failure of the upper part of the slope are mainly multilevel scarps and grooves at the rear of the scarps, which can easily be judged as evidence of potential landslides.

The slope surface bedrock layer survey was carried out from an elevation of 4470 m on the top of the slope to an elevation of 3200 m on the left bank of the Jiangqu River. The survey results show that the steep slope is 205°–285°. In the slope body, the inclination angle is generally 55°–70°. There is no consistent trend of occurrence in the slope rock formation from top to bottom, and the overall rock formation of the slope does not exhibit a characteristic tipping deformation, as depicted in Table 4 and Fig. 18a.

The 200 m range within adit PDG01 with an elevation of 3650 m reveals that the occurrences of massive marbled limestone formations are consistent. In the inclined slope, the inclination angle is generally 60°–75°, and there is no sign of rock layer dumping in the 200 m range of the slope. The inclination angle of the structural surface of the anti-dip slope in exploration PDG01 do not varies with the depth of the cave, as shown in Table 5 and Fig. 18b.

Based on the occurrence of the underlying bedrock layers observed in exploration trenches TC-03 and TC-04, as well as the geological conditions identified through planar geological survey lithology points, there is no clear correlation between the increase in slope of the JRS and elevation. Furthermore, the inclination angle of the structural surface in the flat exploration tunnel of the anti-dip slope do not varies with the cave depth, and there is no discernible pattern of uniformity. Considering the available deep geophysical data, it can be concluded that the current slope generally does not exhibit overall toppling deformation characteristics. The rock mass exposed on the slope has good integrity and relatively high strength and does not have the conditions for toppling deformation. Hence, the presence of reverse slope scarps on the upper portions of the JRS largely eliminates the possibility of overall slope collapse.

4.3.2. Geomorphological evolution analysis considering geological history

On the JRS, the deformation and failure of the upper part of the slope are mainly multilevel scarps and grooves at the rear of the scarps, which can easily be judged as evidence of potential landslides. Based on previous research results on the landform evolution history of the Western Sichuan Plateau Plateau (e.g. Arne et al., 1997; Xu and Kamp, 2000; Kirby et al., 2002) and our field survey of the slope landform, the historical evolution process of the JRS were summarized from a geological age perspective.

The JRS is located in the Sichuan-Tibet alpine valley area, which is one of the six major components of the Qinghai-Tibet Plateau. The general elevation ranges from 3000 m to 5000 m with an average elevation over 4000 m. According to earlier research findings (e.g. Dai and Deng, 2020), the study area witnessed the deposition of multiple carbonate layers from the Paleozoic to the Early Cenozoic. These carbonate formations generally exhibit an east-west trend and are distributed in strip-like patterns. The Late Miocene tectonic activity exerted significant influence, resulting in pronounced folding and faulting in the region. During periods of crustal stability, extensive karstification took place, giving rise to large-scale karst scenarios. Localized karst collapses occurred, leading to the formation of weak areas. The ongoing strong and continuous uplift movement since the Quaternary period has caused the climate to become dry and cold, which has not favored surface karst development. Subsequently, the karstification mainly occurred underground with only a small number of dissolution cracks and karst springs developing on the surface. Especially since the Middle Pleistocene, the exposed bedrock with weak weathering and fresher conditions underwent differential weathering due to varying anti-dissolution capabilities of limestone, mudstone, and dolomite under long-term dissolution and weathering.

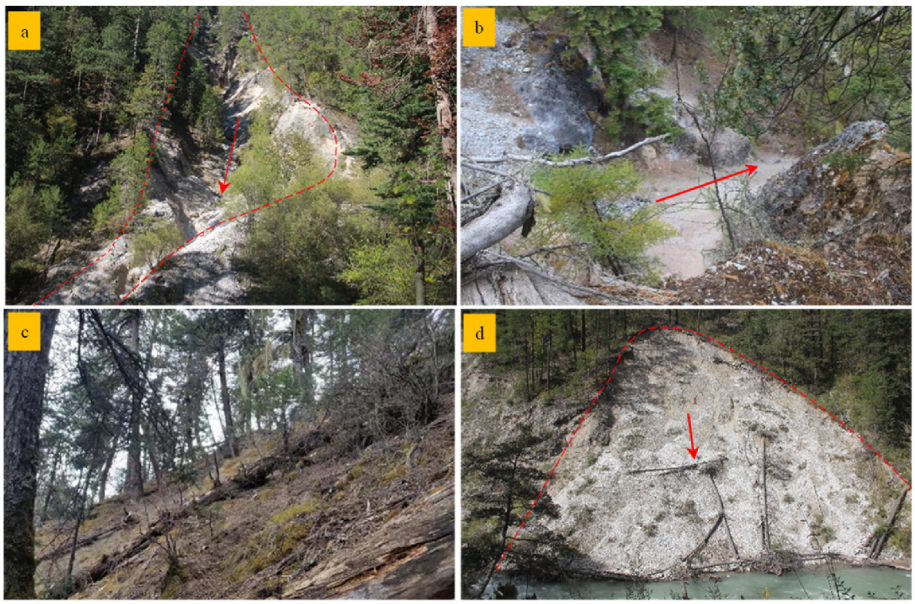

Fig. 11. Photos show the features of some landforms in superficial deformation zone: (a, b) Gullies developed on the slope surface; (c) Sabre tree on the slope surface; and (d) Small-scale superficial landslide at the foot of the slope.

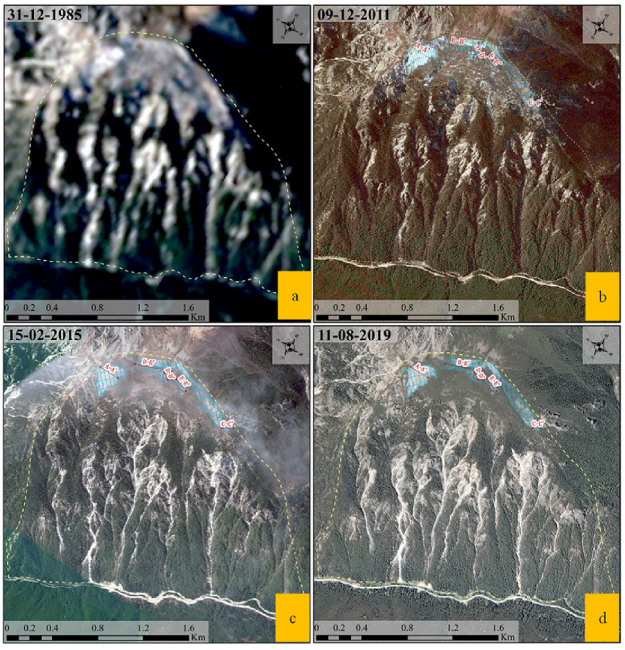

Fig. 12. Remote sensing images from four periods: (a) Shot on December 31, 1985; (b) Shot on December 9, 2011; (c) Shot on February 15, 2015; and (d) Shot on August 11, 2019, from GF-2 satellites.

Limestone and marl bands with low dissolution capacity were more likely to be taken away by dissolution, while dolomites with high dissolution resistance are mostly retained.

The period from the quasi-wide valley to the broad valley (around 100,000–500,000 years ago) corresponds to the secondary planation phase (4100–4600 m) of the Western Sichuan Plateau, which was formed during the Early Pleistocene. During this period, the river downcutting rate was relatively slow and lasted for an extended duration. Following the disintegration of the peneplain, the slope experienced significant deformation. Failure modes during this period may have included sliding failure along the outer or nearly horizontal structural surface of gently inclined slopes, sliding-bending failure along steeply inclined structural surfaces, or toppling failure of shallow surfaces. According to the characteristics of the anti-dip slopes of the rock formations in this area and the extension and distribution of the regional long structural planes (J4: N5°–20°E(W)/NW(SW)∠35°–50°, J5: N5°–20°E(W)/NW(SW)∠60°–85°), it is inferred that local failure geological events with sliding and toppling properties occurred at elevations above approximately 4100 m (see Fig. 19a). During this period, the neotectonic movements in the region were active and strong earthquakes occurred frequently, leading to strong karstification before the Neogene and the formation of karst caves, karst trenches and troughs from differential dissolution. The deformation and destruction of the slope were caused by the overall collapse and subsequent collapse of the stone walls. Following the collapse, a multilevel grooved landform was initially formed (see Fig. 19B). Subsequent weathering, glaciation, denudation, karstification, and freezing and thawing processes further shaped the landform into a grooved and gently undulating slope (see Fig. 19c).

During the Late Pleistocene, the river experienced a period of rapid downcutting, leading to a drop in the erosion base level. As a result, the karst development in the upper part ceased. The only visible features were dissolution fissures below the groundwater erosion base level and the presence of karst springs along these fissures. These springs were only exposed at approximately 170 m–240 m downstream of Huolong ditch and exhibited characteristics of descending springs. Below elevation of 4200 m, the slope shape was smooth and relatively complete. The cracks were mainly of weathered unloading cracks. The shallow surface collapses or collapses locally by erosion due to seasonal rainfall, and there is no excessive deformation or failure (see Fig. 19d and e). This observation is supported by the absence of prominent undulations and gentle slope platforms on the side slopes, as well as the shallow and limited coverage of modern riverbeds and slope toes. Conversely, if rapid deformation and failure occurred above an elevation of 4400 m, or if large-scale instability failure occurred below this elevation, the accumulated instability would undoubtedly be evident at the foot of the slope and in the modern riverbed,

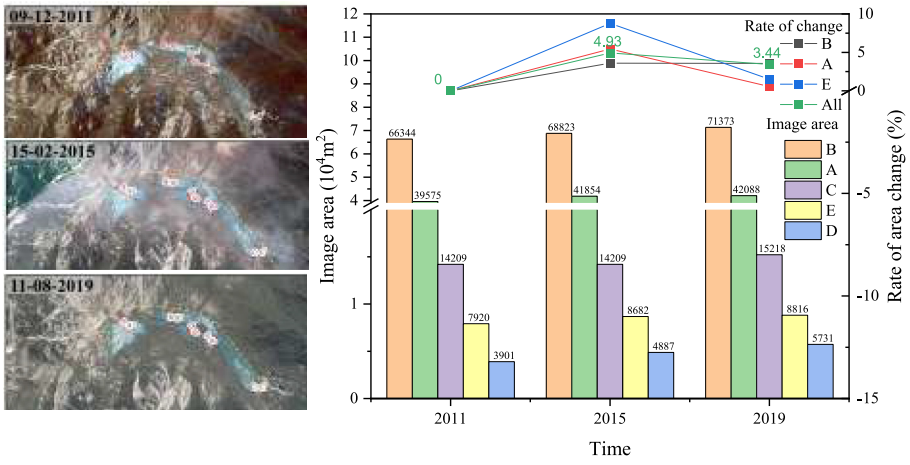

Fig. 13. The area change-rate of remote sensing images from four periods.

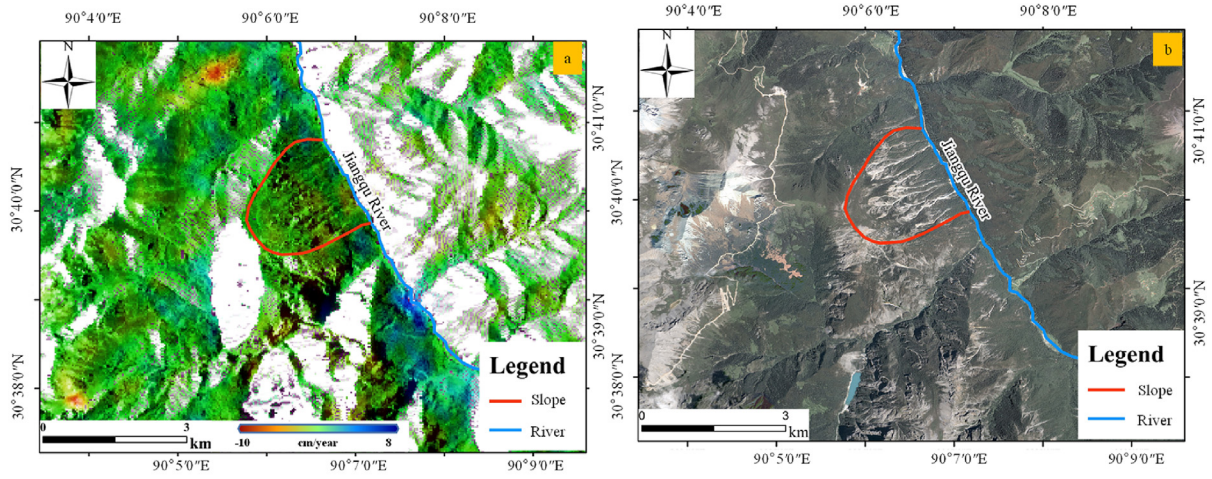

Fig. 14. The SBAS-InSAR time series analysis based on Sentinel-1 data: (a) Result of SBAS-InSAR and (b) image from GF-2 satellites at the same position.

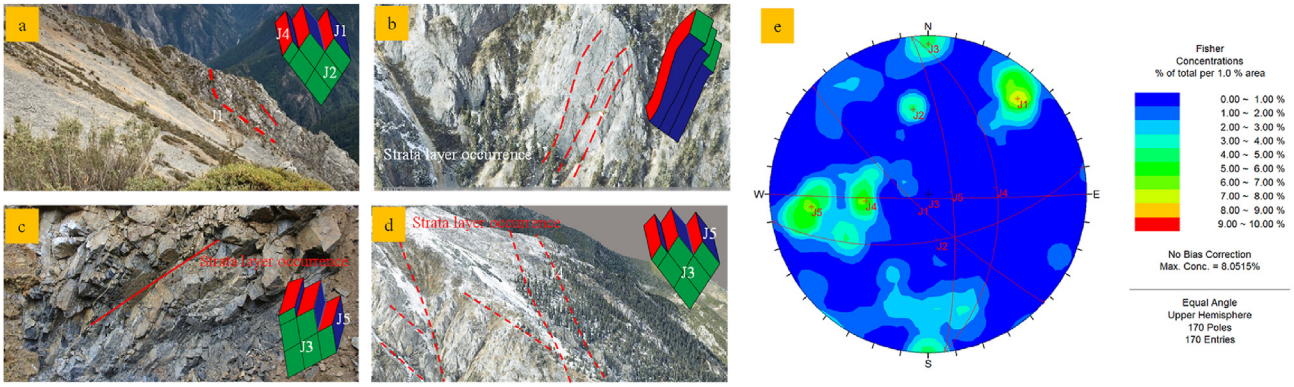

Fig. 15. Dominant joints and cracks that are developed on the JRS: (a) Images of the structural planes (J1, J2, J4); (b) Image of the strata; (c) Photo of the strata and the structural planes (J3, J5); (d) Image of the strata and the structural planes (J3, J5); and (e) Contour diagram of poles for the main joints and cracks in the JRS.

resulting in a significant depth of overburden. In addition, it would even block the Jiangqu River, including large unstable slopes on both sides of the Jiangqu River in the area, and the front edge of the river would be squeezed. Therefore, the deformation of the trailing edge of the slope must occur before the formation of the leading-edge slope.

The Pleistocene in the Quaternary Period was also a period of widespread glaciers. The area was also covered by glaciers (An et al., 2001; Lehmkuhl and Owen, 2005; Zhou et al., 2010; Heyman et al.,

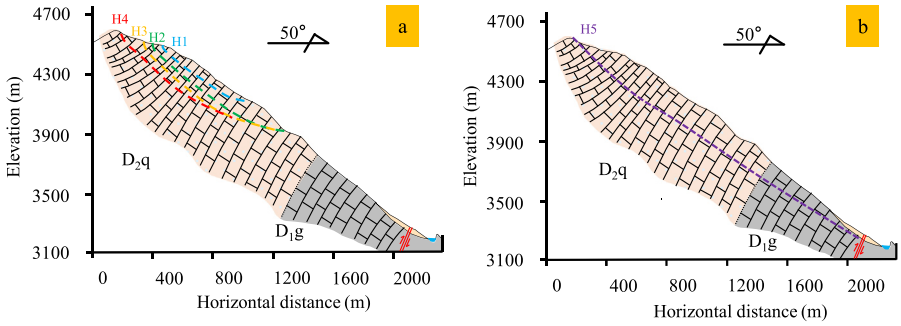

Fig. 16. Sketch map of potential sliding mode: (a) Four shallow sliding surfaces H1–H4, and (b) H5 slip surface considering deep creep.

2011; Kirchner et al., 2011; Wang et al., 2013, 2015; Xu, 2014) (see Fig. 19c). Therefore, the area would have inevitably been influenced by glacier activity. Due to the transformation of intense external geological processes over time, glacial landforms and accumulations have been subjected to varying degrees of erosion and are now largely unrecognizable or destroyed. However, numerous "U"-shaped ice-eroded troughs can still be observed in the region at altitudes of 4200–4800 m, forming a distinct "L"-shape. Specifically, the troughs initially trended northward in the early period and later shifted to an eastward direction (see Fig. 19f). It is speculated that the region was strongly structured in the middle Pleistocene. Similarly, the top of the JRS underwent violent ice erosion to the north during the early-middle Pleistocene, and ice erosion troughs and valleys may also have formed at the early stage at the top ramp of the slope (see Fig. 19c). The sources of material are all on the south and west sides, which are also verification points. Therefore, the initial formation of the complex topography of the moraine floor (see Fig. 19b) led to the development of a fan-shaped landform as it became covered by numerous glacial moraines. The moraine floor's intricate composition resulted in variations in the thickness of the cover. As the river valley continued its downcutting process, the ice tongues suspended at the tops of the four main troughs were pulled downward by gravity, resulting in the formation of multilevel scarps with varying heights. The overlying material lacks schistosity, but distinct, rounded glacial debris can be observed (see Fig. 19g).

4.4. Numerical analysis of aging stability

4.4.1. Current stability

The stability factor of the current slope, calculated using the strength reduction method, is determined to be 1.27. When considering this factor, the potential failure area and potential sliding surface of the slope are depicted in Fig. 20. The potential failure occurs predominantly in tension, while the potential shear failure area is situated along the potential shearing out position of the slope, specifically between elevations of 4000–4150 m and 3700–3800 m. Additionally, a portion of the potential failure area is observed at the foot of the slope due to the presence of a fault and unloading effects. There are two potential sliding surfaces, the first shallow sliding surface is about 50 m deep with shearing out at elevations 3900 m and 3700 m (see Fig. 20b and c), and the second potential sliding surface is about 160 m deep with shearing out at elevation 3600 m (see Fig. 20c). There are multiple levels of potential fracture surfaces at the back edge of the slope (see Fig. 20a), and the potential instability mode of the slope is high instability-sliding mode, and their potential damage ranges are all located above the elevation of 3600 m.

4.4.2. Aging stability

The aging stability calculation is conducted on the time-dependent mechanics results, primarily considering the self-weight effect. Creep calculations are performed for various time durations, including 10, 20, 30, 50, 70, and 100 years. The model, corresponding to each creep duration, is subjected to a strength reduction calculation to determine the stability factors. Additionally, four monitoring points (A1, A2, A3, A4) are established on the slope surface to track the horizontal displacement (see Fig. 20). The total horizontal displacements of the monitoring points and the stability factors under different creep durations are computed and presented in Fig. 21.

As illustrated in Fig. 18a, the total horizontal displacement of each monitoring point remains stable when the stability factor exceeds 1.1. When the stability factor falls between 1.05 and 1.1, indicating a weak deformation stage, the slope deformation begins to increase. A significant increase in slope deformation is observed when the stability factor ranges between 1.03 and 1.05, representing a strong deformation stage. In practical conditions, the stability factor of the slope decreases as deformation progresses, resulting in a continuous change over time. Consequently, the simulation results enable the plotting of a time-displacement curve for the monitoring point, as depicted in Fig. 21b. Analysis of Fig. 21b reveals that the total deformation amount corresponding to the monitoring points remains constant when the stability factor ranges from 1.25 to 1.08. When the stability factor exceeds 1.08, the slope enters a stable creep stage characterized by a leveling off creep deformation, resulting in a stable macroscopic slope deformation. Conversely, when the stability factor falls below 1.08, the displacement of the monitoring point increases significantly, indicating that the slope enters a stage of accelerated deformation where the creep curve fails to reach a stable state. Notably, when the stability factor reaches 1.03, a significant change in the total horizontal deformation amount of the monitoring point occurs, with the appearance of an inflection point in the curve depicted in Fig. 19b. It indicates that creep years need to exceed 80 years for slope deformation to intensify and then form a high level of shallow sliding. Combining the geomorphic features with the stability calculation results, the slope is considered to be a stable slope with landslide geomorphology.

5. Discussion

The advancement of satellite remote sensing technology has led to the widespread adoption of various techniques such as optical remote sensing, LiDAR, InSAR, TLS, and UAV for geohazard identification. These methods have gained significant momentum and have rapidly evolved in recent years (Ferretti et al., 2000; Berardino et al., 2002; Zhang et al., 2012; Hsieh et al., 2016; Mateos et al.,

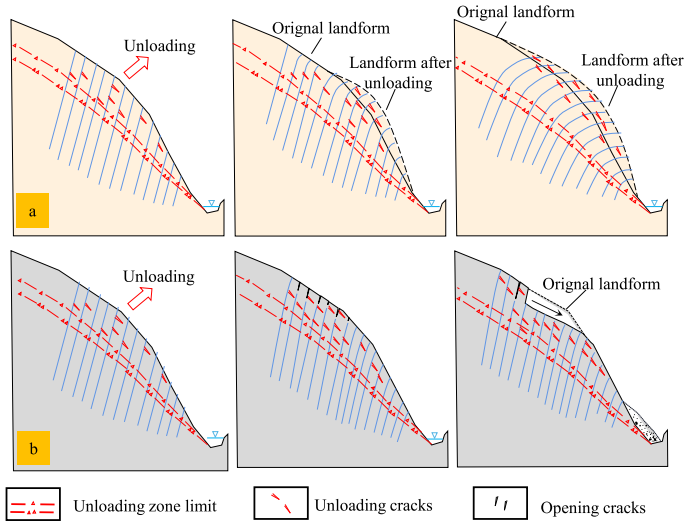

Fig. 17. Two typical slope toppling failure modes: (a) Bending-overturning-toppling failure, and (b) massive toppling failure.

2017; Jia et al., 2019; Li et al., 2020; Xie et al., 2022). The current geomorphological features are frequently considered as the key point that best characterizes whether a slope is a potential landslide. Geomorphological features, especially the chair-shaped terrain and the cracks and scarps generated on the trailing edge, are the most commonly used landslide identification evidence when using remote sensing images to identify landslides. The presence of landslide geomorphological features frequently leads to the assumption that slopes are more likely to be potential landslides, in contrast to slopes without such features. This judgment method is typically effective in areas where the geomorphological causes are straightforward and influenced by single factors (Scaioni et al., 2014; Fan et al., 2017; Intrieri et al., 2018; Ouyang et al., 2018; Li et al., 2019). However, the Qinghai-Tibet Plateau is an area with complex geological environment and strong tectonic activities. The formation of the landform is affected by strong tectonic effects such as glaciers, freeze-thaw, karst, weathering, and unloading, etc., instead of being solely affected by the erosion of river. Numerous slopes exhibiting landslide geomorphology are primarily shaped by intricate external conditions, yet they remain stable slopes rather than potential landslides. The JRS investigated in this study exemplifies a stable slope with landslide geomorphology, and similar examples abound across the Qinghai-Tibet Plateau.

While features like chair-shaped terrain, presence of cracks, and scarps on the trailing edge are frequently associated with landslide geomorphology, it is important to note that their presence does not guarantee the classification of a slope as a potential landslide. Conversely, slopes that do have the potential for landslides may not exhibit the characteristic chair-shaped terrain or prominent cracks

Table 4
The statistical table of the occurrence of the rock formation exposed on the slope surface with elevation change.

No.	Geographic coordinates		Elevation (m)	True angle of dip (°)	Apparent angle of dip (°)	Stratigraphic occurrence
1	N 30°40′22.40″	E 99°06′54.91″	3200	47	47	N30°W/ SW∠47°
2	N 30°40′16.11″	E 99°06′56.41″	3220	68	67	N25°W/ SW∠68°
3	N 30°40′07.72″	E 99°06′49.69″	3333	55	51	N70°W/ SW∠55°
4	N 30°40′07.72″	E 99°06′46.60″	3390	64	62	N65°W/ SW∠64°
5	N 30°40′05.20″	E 99°06′44.43″	3461	63	62	N20°W/ SW∠63°
6	N 30°40′07.59″	E 99°06′41.96″	3477	40	38	N20°W/ SW∠40°
7	N 30°40′04.13″	E 99°06′41.96″	3520	67	65	N15°W/ SW∠67°
8	N 30°40′02.94″	E 99°06′42.89″	3522	45	30	N15°E/ NW∠45°
9	N 30°39′39.30″	E 99°06′04.73″	4433	55	54	N30°W/ SW∠55°
10	N 30°39′55.87″	E 99°05′58.24″	4440	64	64	N38°W/ SW∠64°
11	N 30°39′54.63″	E 99°05′57.16″	4455	70	69	N22°W/ SW∠70°
12	N 30°39′47.85″	E 99°05′52.72″	4470	55	44	N7°E/ SE∠55°

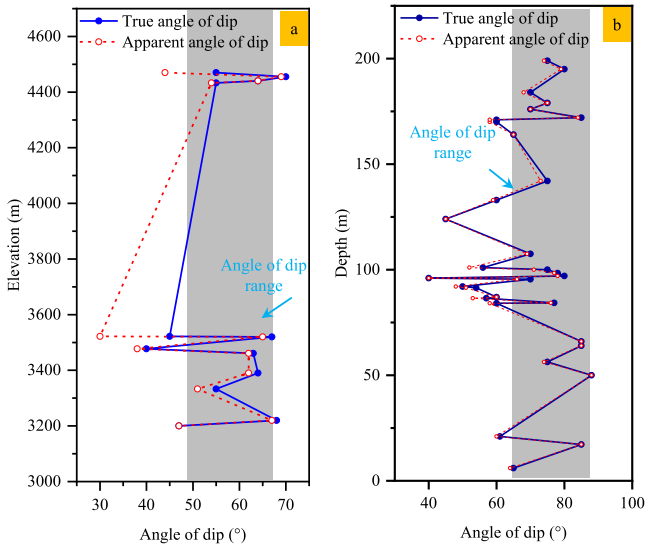

Fig. 18. (a) The statistical graph of the rock formation occurrence exposed on the slope surface with elevation change, and (b) Statistical diagram of the rock formation occurrence with horizontal burial depth changes (according to the statistical data in adit PDG01).

Table 5
The statistical table of the rock formation occurrence with horizontal burial depth change (according to the statistical data in adit PDG01).

No.	Hole depth position (m)	True angle of dip (°)	Apparent angle of dip (°)	Stratigraphic occurrence
1	6	65	64	N25°W/SW∠65°
2	17.2	85	85	N38°W/SW∠85°
3	21	61	60	N30°W/SW∠61°
4	50	88	88	N25°W/SW∠88°
5	56.3	75	74	N18°W/SW∠75°
6	64	85	85	N40°W/SW∠85°
7	66	85	85	N57°W/SW∠85°
8	84.1	60	58	N60°W/SW∠60°
9	84.3	77	76	N20°W/SW∠77°
10	86.5	57	53	N10°W/SW∠57°
11	87	60	60	N35°W/SW∠60°
12	91.4	54	51	N65°W/SW∠54°
13	92	50	48	N20°W/SW∠50°
14	95.5	70	66	N75°W/SW∠70°
15	96	40	40	N30°W/SW∠40°
16	97	80	78	N70°W/SW∠80°
17	98.4	78	77	N65°W/SW∠78°
18	100	75	71	N80°W/SW∠75°
19	101	56	52	N10°W/SW∠56°
20	107.5	70	69	N25°W/SW∠70°
21	124	45	45	N50°W/SW∠45°
22	133	60	59	N26°W/SW∠60°
23	142	75	73	N70°W/SW∠75°
24	164	65	65	N30°W/SW∠65°
25	170	60	58	N20°W/SW∠60°
26	171	60	58	N60°W/SW∠60°
27	172	85	84	N65°W/SW∠85°
28	176	70	70	N40°W/SW∠70°
29	179	75	75	N50°W/SW∠75°
30	184	70	68	N15°W/SW∠70°
31	195	80	79	N15°W/SW∠80°
32	199	75	74	N65°W/SW∠75°

and scarps on the trailing edge. In their study on the history of deformation of large-scale rock landslides and its implications, Li et al. (2019) highlighted that the presence and development of trailing edge cracks and front edge slumping varied in different types of landslides. For bedding landslides such as Yingping Village landslide and Xinmo Village landslide (Fan et al., 2017; Intrieri et al., 2018), the deformation process did not exhibit significant trailing edge crack development and front edge slumping. In contrast, for anti-dipping landslides like Pusa Village landslide and magmatic rock landslides such as Su Village landslide and Baige landslide (Ouyang et al., 2018), the trailing edge cracks extended continuously until closure, while the front edge deformation primarily involved increasing-scale collapses, indicating a coordinated deformation pattern. As for the JRS, the trailing edge is historically deformed which is caused by glaciers, freeze-thaw, karst, weathering and unloading, and the leading edge does not have a coordinated deformation. It is easy to consider JRS as a potential landslide without distinguishing its deformation history through the analysis of evolution history. It can be seen that a slope with landslide geomorphology is not necessarily a potential landslide, and a potential landslide does not necessarily have the typical features of a landslide.

Hence, this study employs a process-oriented method that incorporates the concept of time-dependent evolution to assess the potential landslide status of the slope. Unlike the remote sensing approach that primarily relies on geomorphic features, this method recognizes the significance of considering the temporal aspect in evaluation. In the quantitative calculation phase, a time-dependent stability assessment method is introduced, which encompasses time-dependent mechanical calculations and strength reduction analyses tailored for anticline slopes. This method, in contrast to the remote sensing approach, underscores the crucial role of time-dependent evolution and facilitates a comprehensive process encompassing qualitative analysis and quantitative calculation.

However, there are still limitations in the quantitative calculation part that may lead to less accurate calculation results. When considering the strain-softening process in the model, it is simplified to the process of linear variation of strength with strain (Wang and Zhao, 2016), which is different from the actual variation

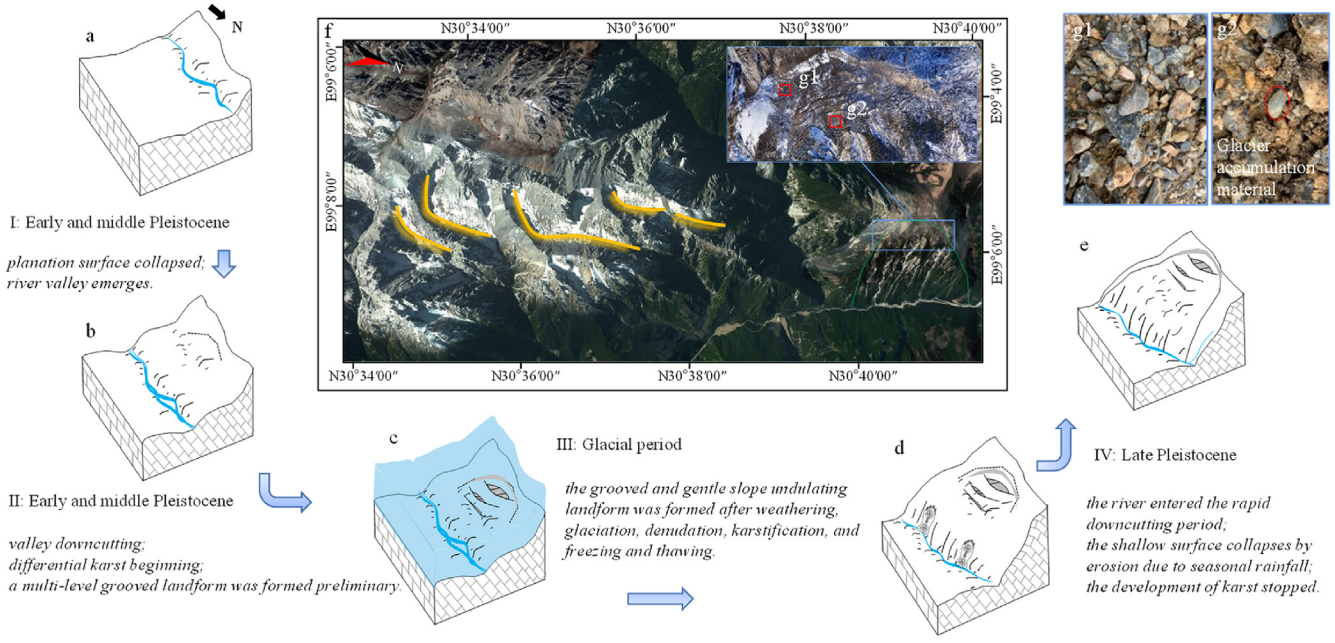

Fig. 19. Schematic diagram of historical changes in the landform of the JRS: (a, b) From the early Pleistocene to the middle Pleistocene, the planation surface collapsed, and the slope deformed; (c) Glacier development during the Pleistocene; (d) In the late Pleistocene, rivers rapidly cut down, and the development of karst stopped; (e) Current round, chair-like and multilevel gentle slope ridges and alternating groove landforms; and (f, g) Glacial landforms in the area and gravel-like material.

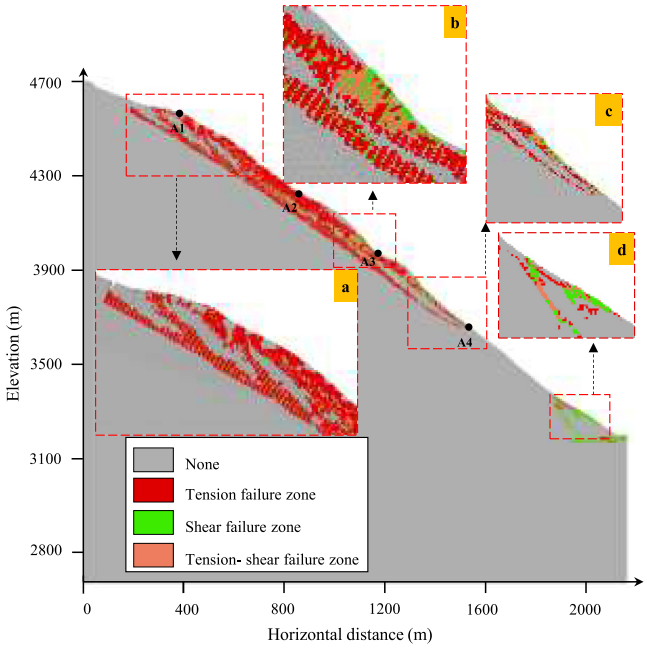

Fig. 20. State diagram of the damage zone of the slope when the discount factor $K_s = 1.27$: (a) Multiple levels of potential fracture surfaces at the back edge of the slope; (b) Shearing out location of shallow sliding surfaces; (c) Shearing out position of deep sliding surface; and (d) Area affected by fracture at the foot of the slope.

process, thus the corresponding rheological intrinsic model needs further improvement. In the simulation calculation, the model was simplified by considering the optimization of calculation speed, and only the influence of the layers was considered, without considering the influence of factors such as the joints surface. The 3D stability accnalysis based on the actual survey results is more reasonable and closer to the actual situation, which is also worth exploring. In the analysis of aging stability, a stepwise reduction of strength parameters is conducted, leading to the derivation of a new set of discounted strength values. Subsequently, numerical calculations are performed to gradually approach the limit equilibrium state of the slope. The coefficient of reduction achieved at this stage is considered as the stability coefficient. However, in the process of slope failure, there are differences in the degree and speed of decay of cohesion and internal friction angle. Therefore, the experimental study on the weakening law of cohesion and internal friction angle may reflect more accurately the real trend of aging stability of slopes.

The whole process method emphasizes the importance of time-dependent evolution more than the conventional method, and also incorporates the quantitative calculation part, thus avoiding the over-emphasis on the geomorphological features. However, the method is only applied to the JRS with landslide features, which is located on the Tibetan Plateau.

6. Conclusions

The JRS, a controlled slope located on the Qinghai-Tibet Plateau, exhibits characteristic geomorphological features commonly associated with landslides. Recognizing the limitations of relying solely on remote sensing methods for landslide identification, a process-oriented method considering time-dependent evolution was employed to assess the potential for landslide occurrence. The findings of this study are summarized as follows:

(1) The geomorphological features are frequently considered the most direct evidence of landslides. Nevertheless, excessive emphasis on geomorphological features will result in misjudgment. The combined method of comprehensive remote sensing, geology, and numerical analysis is a process from qualitative analysis to quantitative calculation. Within this framework, the concept of time-dependent evolution is central to the analysis and calculation of aging stability, providing a deeper understanding of the historical evolution of the slope. By utilizing this method, the potential misjudgment associated with remote sensing methods that overly emphasize geomorphological features can be effectively mitigated.

(2) The comprehensive remote sensing analysis by UAV, remote sensing and InSAR indicates that JRS may be a potential landslide. This study has identified and proposed two potential instability modes based on geomorphological features. However, the comprehensive geology analysis, conducted through historical evolution analysis and rock structure analysis, refutes the possibility of these two instability modes. In contrast, the numerical analysis provides

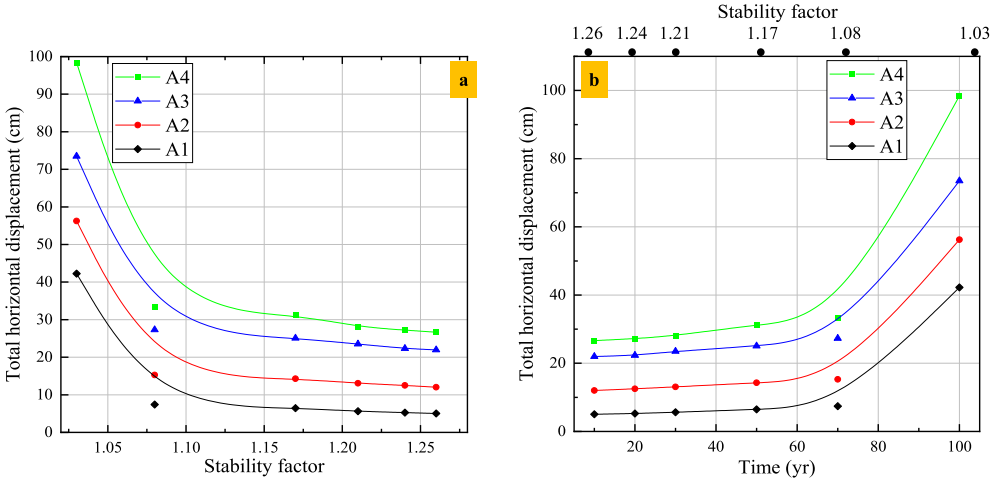

Fig. 21. Calculation results of aging stability: (a) The total horizontal displacement of each monitoring point, and (b) Elapsed time versus total horizontal displacement curve.

quantitative support for the slope's stability by evaluating both the current stability and aging stability. The results indicate that creep slopes would require more than 80 years to potentially exhibit shallow sliding.

(3) The JRS is considered to be a stable anti-dip slope with typical landslide landforms rather than a potential large-scale rocky landslide. Its distinctive geomorphological features, resembling those of landslides, are the characteristic and representative of the entire Qinghai-Tibet Plateau and other deep incline valley regions. This work provides insights into the geomorphological characterization and evolution history of the JRS, as well as useful inspiration for the study of other slopes with similar landslide geomorphology.

Declaration of competing interest

The authors declare that they have no known competing financial interests or personal relationships that could have appeared to influence the work reported in this paper.

Acknowledgments

This research was supported by the National Natural Science Foundation of China (Grant Nos. 41972284 and 42090054). This work was also supported by the State Key Laboratory of Geohazard Prevention and Geoenvironment Protection Independent Research Project (Grant No. SKLGP2020Z005).

References

An, Z.S., Kutzbach, J.E., Prell, W.L., et al., 2001. Evolution of asian monsoons and phased uplift of the Himalaya-Tibetan Plateau since late Miocene times. Nature 411 (6833), 62–66.
Arne, D., Worley, B., Wilson, C.H., et al., 1997. Differential exhumation in response to episodic thrusting along the eastern margin of the Tibetan plateau. Tectonophysics 280, 239–256.
Berardino, P., Fornaro, G., Lanari, R., 2002. A new algorithm for surface deformation monitoring based on small baseline differential SAR interferograms. IEEE Trans. Geosci. Rem. 40 (11), 2375–2383.
Cai, F.L., Ding, L., Andrew, K.L., et al., 2016. Late triassic paleogeographic reconstruction along the neo-Tethyan ocean margins, southern Tibet. Earth Planet. Sc. Lett. 435 (1), 105–114.
Cai, Y.J., Cheng, H.Y., Wu, S.F., et al., 2020. Breaches of the Baige barrier Lake: emergency response and dam breach flood. Sci. China Technol. Sci. 63 (2), 571–584.
Caine, N., 1982. Toppling failures from alpine cliffs on ben Lomond, Tasmania. Earth. Surf. Proc. Land. 7 (2), 133–152.
Chen, G.Q., Li, H., Wei, T., et al., 2021. Searching for multistage sliding surfaces based on the discontinuous dynamic strength reduction method. Eng. Geol. 286, 106086.
Cho, N., Martin, C.D., Sego, D.C., 2007. A clumped particle model for rock. Int. J. Rock Mech. Min. 44 (7), 997–1010.
Cruden, D.M., Hu, X., Lu, Z., 1993. Rock topples in the highway cut west of Clairvaux, Jasper, Alberta. Can. Geotech. J. 30 (6), 1016–1023.
Cui, P., Su, F.H., Zou, Q., et al., 2015. Risk assessment and disaster reduction strategies for mountainous and meteorological hazards in Tibetan Plateau. Chin. Sci. Bull. 60 (32), 3067–3077 (in Chinese).
Dai, F.C., Deng, J.H., 2020. Development characteristics of landslide hazards in three-rivers basin of Southeast Tibetan plateau. Adv. Eng. Sci. 52 (5), 3–15 (in Chinese).
De Freitas, M.H., Watters, R.J., 1973. Some field examples of toppling failure. Geotechnique 23 (4), 495–514.
Ding, L., Spicer, R.A., Yang, J., et al., 2017. Quantifying the rise of the Himalaya orogen and implications for the South Asian monsoon. Geology 45 (3), 215–218.
Fan, X.M., Xu, Q., Scaringi, G., et al., 2017. Failure mechanism and kinematics of the deadly June 24th 2017 Xinmo landslide, Maoxian, sichuan, China. Landslides 14 (6), 2129–2146.
Fan, X.M., Dufresne, A., Whiteley, J., et al., 2021. Recent technological and methodological advances for the investigation of landslide dams. Earth Sci. Rev. 218, 103646.
Ferretti, A., Prati, C., Rocca, F., 2000. Nonlinear subsidence rate estimation using permanent scatterers in differential SAR interferometry. IEEE Trans. Geosci. Rem. 38, 2202–2212.
Gu, D.M., Huang, D., 2016. A complex rock topple-rock slide failure of an anaclinal rock slope in the Wu Gorge, Yangtze River, China. Eng. Geol. 208, 165–180.
Guo, Q., Pang, Z., Wang, Y., et al., 2017. Fluid geochemistry and geo thermometry applications of the Kangding high-temperature geothermal system in Eastern Himalayas. Appl. Geochem. 81, 63–75.
Guo, C.B., Wu, R.A., Li, X., et al., 2020. Developmental characteristics and formation mechanism of the Rizha potential giant rock landslide, western sichuan province, China. J. Eng. Geol. 28 (4), 772–783 (in Chinese).
Heyman, J., Stroeven, A.P., Caffee, W.M., et al., 2011. Palaeoglaciology of Bayan Har Shan, NE Tibetan Plateau: exposure ages reveal a missing LGM expansion. Quat. Sci. Rev. 30, 1988–2001.
Hsieh, Y.C., Chan, Y.C., Hu, J.C., 2016. Digital elevation model differencing and error estimation from multiple sources: a case study from the Meiyuan Shan landslide in Taiwan. Rem. Sens. 8 (3), 199.
Huang, R.Q., 2012. Mechanisms of large-scale landslides in China. Bull. Eng. Geol. Environ. 71, 161–170.
Intrieri, E., Raspini, F., Fumagalli, A., et al., 2018. The Maoxian landslide as seen from space: detecting precursors of failure with Sentinel-1 data. Landslides 15 (1), 123–133.
Itasca Consulting Group Inc, 2005. FLAC3D: Fast Lagrangian ANALYSIS of Continua in 3 Dimensions User Manual (Version3.0). Consulting Group Inc., Minneapolis.
Ji, S.P., Yu, D.W., Shen, C.Y., et al., 2020. Landslide detection from an open satellite imagery and digital elevation model dataset using attention boosted convolutional neural networks. Landslides 17 (6), 1337–1352.
Jia, B., Wu, Z., Du, Y., 2019. Real-time stability assessment of unstable rocks based on fundamental natural frequency. Int. J. Rock Mech. Min. 124, 104134.
Jiang, G.Z., Hu, S.B., Shi, Y.Z., et al., 2019. Terrestrial heat flow of continental China: updated dataset and tectonic implications. Tectonophysics 753, 36–48.
Kirby, E., Reiners, P.W., Krol, M.A., et al., 2002. Late cenozoic evolution of the eastern margin of the Tibetan plateau: inferences from 40ar/39ar and (u-th)/he thermochronology. Tectonics 21 (1).
Kirchner, N., Greve, R., Stroeven, A.P., et al., 2011. Paleoglaciological reconstructions for the Tibetan Plateau during the last glacial cycle: evaluating numerical ice sheet simulations driven by GCM-ensembles. Quat. Sci. Rev. 30, 248–267.
Kuang, X., Jiao, J., 2016. Review on climate change on the Tibetan Plateau during the last half century. J. Geophys. Res. Atmos. 121, 3979–4007.
Lehmkuhl, F., Owen, L.A., 2005. Late Quaternary glaciation of Tibet and the bordering mountains: a review. Boreas 34 (2), 87–100.
Li, W.L., Xu, Q., Lu, H.Y., et al., 2019. Tracking the deformation history of large-scale rocky landslides and its enlightenment. Geomatics Inf. Sci. Wuhan Univ. 44 (7), 1043–1053 (in Chinese).
Li, M.H., Zhang, L., Ding, C., et al., 2020. Retrieval of historical surface displacements of the Baige landslide from time-series SAR observations for retrospective analysis of the collapse event. Rem. Sens. Environ. 240, 111695.
Lu, C., Cai, C., 2019. Challenges and countermeasures for construction safety during the Sichuan-Tibet railway project. Engineering 5 (5), 833–838.
Mao, X., Zhu, D., Ndikubwimana, I., et al., 2021. The mechanism of high-salinity thermal groundwater in Xinzhou geothermal field, South China: insight from water chemistry and stable isotopes. J. Hydrol. 593, 125889.
Mateos, R.M., Azañón, J.M., Roldán, F.J., et al., 2017. The combined use of PSInSAR and UAV photogrammetry techniques for the analysis of the kinematics of a coastal landslide affecting an urban area (SE Spain). Landslides 14 (2), 743–754.
Metternicht, G., Hurni, L., Gogu, R., 2005. Remote sensing of landslides: an analysis of the potential contribution to geo-spatial systems for hazard assessment in mountainous environments. Rem. Sens. Environ. 98, 284–303.
Nichol, J.E., Shaker, A., Wong, M.S., 2006. Application of high-resolution stereo satellite images to detailed landslide hazard assessment. Geomorphology 76, 68–75.
Ning, Y.B., Tang, H.M., Smith, J.V., et al., 2021. Study of the in situ stress field in a deep valley and its influence on rock slope stability in Southwest China. Bull. Eng. Geol. Environ. 80 (4).
Niu, F.J., Luo, J., Lin, Z.J., et al., 2016. Thaw-induced slope failures and stability analyses in permafrost regions of the Qinghai-Tibet Plateau, China. Landslides 13, 55–65.
Ouyang, C.J., Zhao, W., Xu, Q., et al., 2018. Failure mechanisms and characteristics of the 2016 catastrophic rockslide at Su village, Lishui, China. Landslides 15 (7), 1391–1400.
Prakash, N., Manconi, A., Loew, S., 2020. Mapping landslides on EO data: performance of deep learning models vs. traditional machine learning models. Rem. Sens 12 (3), 346.
Qi, S.W., Wu, F.Q., Yan, F.Z., et al., 2004. Mechanism of deep cracks in the left bank slope of Jinping first stage hydropower station. Eng. Geol. 73, 129–144.
Scaioni, M., Longoni, L., Meillo, V., et al., 2014. Remote sensing for landslide investigations: an overview of recent achievements and perspectives. Rem. Sens 6 (10), 9600–9652.
Shang, Y.J., Yang, Z.F., Li, L.H., et al., 2003. A super-large landslide in Tibet in 2000: background, occurrence, disaster, and origin. Geomorphology 54 (3), 225–243.
Sun, Z., Ma, R., Wang, Y., et al., 2016. Using isotopic, hydrogeochemical tracer and temperature data to characterize recharge and flow paths in a complex karst groundwater flow system in Northern China. Hydrogeol. J. 24 (6), 1393–1412.
Sun, X., Chen, G.Q., Huang, M.Y., et al., 2023. Method for analyzing the evolution characteristics of in-situ stress field considering rheology and degradation: a deeply incised valley in Qinghai-Tibet Plateau, case study. Eng. Geol. 315, 107029.
Tamrakar, N., Yokota, S., Osaka, O., 2002. A toppled structure with sliding in the Siwalik Hills, midwestern Nepal. Eng. Geol. 64, 339–350.

Tapponnier, P., Molnar, P., 1977. Active faulting and tectonics in China. J. Geophys. Res. 82 (20), 2905–2930.
Tu, G.X., Deng, H., 2020. Characteristics of a deep-seated flexural toppling fracture and its relations with downcutting by the Lancang River: a case study on a steeply dipping layered rock slope, Southwest China. Eng. Geol. 275, 105754.
Wang, B., Ma, Q., 1986. Boundary element analysis methods for ground stress field of rock masses. Comput. Geotech. 2 (5), 261–274.
Wang, J., Kassab, C., Harbor, J.M., et al., 2013. Cosmogenic nuclide constraints on late Quaternary glacial chronology on the Dalijia Shan, northeastern Tibetan Plateau. Quat. Res. 79 (3), 439–451.
Wang, J., Cui, H., Harbor, J.M., et al., 2015. Mid-MIS3 climate inferred from reconstructing the Dalijia Shan ice cap, North-Eastern Tibetan Plateau. J. Quat. Sci. 30 (6), 558–568.
Wang, H., Zhao, W.J., 2016. A study on initial geostress field of rock masses in valley zone. Int. J. Simul. Syst. Sci. Technol. 17 (48), 12, 1–12.8.
Wang, H., Li, K.J., Chen, L.C., et al., 2020. Evidence for holocene activity on the Jiali fault, an active block boundary in the Southeastern Tibetan Plateau. Seismol Res. Lett. 91 (3), 1776–1780.
Wang, D.P., Zhou, Y., Pei, X.J., et al., 2021. Dam-break dynamics at Huohua lake following the 2017 Mw 6.5 Jiuzhaigou earthquake in sichuan, China. Eng. Geol. 289, 106145.
Wang, G.J., Zhao, B., Wu, B.S., et al., 2023. Intelligent prediction of slope stability based on visual exploratory data analysis of 77 in situ cases. Int. J. Min. Sci. Technol. 33 (1), 49–61.
Woodward, R.C., 1988. The investigation of toppling slope failures in welded ash flow tuff at Glennies Creek Dam, New South Wales. Q. J. Eng. Geol. 21, 289–298.
Wyllie, D.C., 1980. Toppling rock slope failures examples of analysis and stabilization. Rock Mech. Rock Eng. 13 (2), 89.
Xie, M., Du, Y., Jiang, Y., et al., 2022. Editorial: rock landslide risk assessment, stability analysis and monitoring for the development of early warning systems and reinforcement measures. Front. Earth Sci. 10, 1118991.
Xu, G.Q., Kamp, P.J.J., 2000. Tectonics and denudation adjacent to the Xianshuihe Fault, eastern Tibetan Plateau: constraints from fission track thermochronology. J. Geophys. Res. Solid Earth 105 (B8), 19231–19251.
Xu, X.K., 2014. Climates during late Quaternary glacier advances: glacier-climate modeling in the Yingpu Valley, eastern Tibetan Plateau. Quat. Sci. Rev. 101, 18–27.
Xu, C., Xu, X., Shen, L., et al., 2016. Optimized volume models of earthquake-triggered landslides. Sci. Rep. 6 (1), 29797.
Yang, R., Fellin, M.G., Herman, F., et al., 2016. Spatial and temporal pattern of erosion in the three rivers region, southeastern Tibet. Earth Planet. Sc. Lett. 433, 10–20.
Zhang, P.Z., Shen, Z., Wang, M., et al., 2004. Continuous deformation of the Tibetan Plateau from global positioning system data. Geology 32 (9), 809–812.
Zhang, L., Lu, Z., Ding, X.L., et al., 2012. Mapping ground surface deformation using temporarily coherent point SAR interferometry: application to Los Angeles Basin. Rem. Sens. Environ. 117, 429–439.
Zhang, Z.L., Liu, G., Wu, S.R., et al., 2015. Rock slope deformation mechanism in the Cihaxia hydropower station, northwest China. Bull. Eng. Geol. Environ. 74 (3), 943–958.
Zhang, H., Oskin, M.E., Liu, Z., et al., 2016. Pulsed exhumation of interior eastern Tibet: implications for relief generation mechanisms and the origin of high-elevation planation surfaces. Earth Planet. Sc. Lett. 449, 176–185.
Zhang, Z.Q., Wu, Q.B., Jiang, G.L., et al., 2020. Changes in permafrost temperatures from 2003 to 2015 on the Qinghai-Tibet Plateau. Cold Reg. Sci. Technol. 169, 102904.
Zhao, H., Ma, F., Xu, J., Guo, J., 2012. In situ stress field inversion and its application in mining-induced rock mass movement. Int. J. Rock Mech. Min. Sci. 53, 120–128.
Zhou, S.Z., Wang, J., Xu, L.B., et al., 2010. Glacial advances in southeastern Tibet during late Quaternary and their implications for climatic changes. Quatern. Int. 218, 58–66.

Guoqing Chen, Professor, received his PhD from Institute of Rock and Soil Mechanics, Chinese Academy of Sciences in 2009. He conducted research on the stability of rocky slopes at the Postdoctoral Station of Geological Resources and Geological Engineering of Chengdu University of Technology from 2010 to 2015. He received the Sichuan Provincial Outstanding Youth Fund in 2014, and was selected as the reserve candidate of Academic and Technical Leaders of Sichuan Province in the same year. He was promoted to a professor in 2015, and received the Gu Dezhen Youth Science and Technology Award in 2016. His main research interests include: (1) Testing technology of laboratory large-scale rock samples and physical models; (2) Time-dependent deformation failure of large rocky slopes and landslide prevention and control; and (3) Prevention and control of high-stress deep-engineering hazards. His major research achievements include: (1) Pioneering the theory of heterogeneous rheological failure of geotechnical bodies; (2) Proposing the dynamic strength reduction method for progressive slope failure; (3) Developing the geomechanical theory of locked segments of rocky slopes; and (4) Optimizing the catastrophic mechanism of geotechnical bodies in the extreme geological environment of the Qinghai-Tibet Plateau.